© 2014. Published by The Company of Biologists Ltd | Journal of Cell Science (2014) 127, 1279–1292 doi:10.1242/jcs.140756

RESEARCH ARTICLE

The inverse BAR domain protein IBARa drives membrane remodeling to control osmoregulation, phagocytosis and cytokinesis

Joern Linkner[1,*], Gregor Witte[2,*,‡], Hongxia Zhao[3], Alexander Junemann[1], Benjamin Nordholz[1], Petra Runge-Wollmann[2], Pekka Lappalainen[3] and Jan Faix[1,*,‡]

ABSTRACT

Here, we analyzed the single inverse Bin/Amphiphysin/Rvs (I-BAR) family member IBARa from *Dictyostelium discoideum*. The X-ray structure of the N-terminal I-BAR domain solved at 2.2 Å resolution revealed an all-α-helical structure that self-associates into a 165-Å zeppelin-shaped antiparallel dimer. The structural data are consistent with its shape in solution obtained by small-angle X-ray scattering. Cosedimentation, fluorescence anisotropy, and fluorescence and electron microscopy revealed that the I-BAR domain bound preferentially to phosphoinositide-containing vesicles and drove the formation of negatively curved tubules. Immunofluorescence labeling further showed accumulation of endogenous IBARa at the tips of filopodia, the rim of constricting phagocytic cups, in foci connecting dividing cells during the final stage of cytokinesis and most prominently at the osmoregulatory contractile vacuole (CV). Consistently, IBARa-null mutants displayed defects in CV formation and discharge, growth, phagocytosis and mitotic cell division, whereas filopodia formation was not compromised. Of note, IBARa-null mutants were also strongly impaired in cell spreading. Taken together, these data suggest that IBARa constitutes an important regulator of numerous cellular processes intimately linked with the dynamic rearrangement of cellular membranes.

KEY WORDS: Autophagy, Contractile vacuole, Cytokinesis, *Dictyostelium discoideum*, Filopodia, Phagocytosis, Inverse BAR domain, IBARa, Membrane dynamics

INTRODUCTION

Numerous cellular processes including endocytosis and cell migration or division require the dynamic remodeling of the plasma membrane and the underlying actin cytoskeleton (Keren, 2011). Members of the superfamily of Bin/Amphipysin/Rvs (BAR)-domain proteins are characterized by their ability to sculpt membranes after their recruitment and clustering by acidic phospholipids (Saarikangas et al., 2010; Qualmann et al., 2011). BAR domains are grouped into three subfamilies: BAR and F-BAR domain proteins, in combination with actin polymerization, have been shown to be key players in initiating and stabilizing endosomal vesicles by generating positive membrane curvature and bending the plasma membrane inwards (Peter et al., 2004; Frost et al., 2008), whereas the subfamily of the inverse BAR domain (I-BAR) proteins induce negative membrane curvature to promote cell protrusions (Millard et al., 2005; Suetsugu et al., 2006a; Mattila et al., 2007; Saarikangas et al., 2009).

The mammalian I-BAR domain protein family comprises the five members IRSp53 (also known as BAIAP2), MIM (MTSS1), ABBA (MTSS1L), IRTKS (BAIAP2L1) and Pinkbar (BAIAP2L2), which additionally harbor protein–protein interaction modules such as CRIB, SH3 or actin-monomer-binding WH2-domains that link them to signaling pathways or directly to actin-based processes (Scita et al., 2008; Pykäläinen et al., 2011). Previous studies have suggested that I-BAR proteins regulate the formation of actin protrusions through interactions with membranes, actin and other cytoskeletal regulators, for instance as described for IRSp53 with VASP (Vaggi et al., 2011), or the Diaphanous-related formin mDia1 and the Scar/WAVE-complex subunit WAVE2 (Goh et al., 2011). In addition, pathogens such as enterohaemorrhagic *Escherichia coli* (EHEC) use these interactions to recruit the actin-assembly machinery for the formation of actin pedestals (de Groot et al., 2011). Although the precise functions of IRSp53 and MIM have not yet been fully resolved, both proteins have been proposed to link Arp2/3-complex-mediated actin assembly with the formation of cell protrusions. Notably, IRSp53 interacts with the small GTPases Cdc42 and Rac through its N-terminal region and with WAVE2 through its central SH3 domain (Krugmann et al., 2001). Consequently, IRSp53 has been suggested to regulate the activity of the Arp2/3 complex through interaction with the WAVE complex and to be involved in lamellipodia and filopodia formation (Nakagawa et al., 2003; Biyasheva et al., 2004; Suetsugu et al., 2006b). In mice, IRSp53 deficiency leads to defects in the development of the eye and central nervous system and in the formation of filopodia (Kim et al., 2009; Sawallisch et al., 2009; Chauhan et al., 2009; Disanza et al., 2013). MIM was originally identified as a putative tumor suppressor because it is expressed in nonmetastatic cancer cells but is absent from metastatic ones (Lee et al., 2002). Knockout studies have revealed that MIM functions at the interface of the plasma membrane and the actin cytoskeleton to promote the maintenance of intercellular junctions in epithelial tissues and that it contributes to B-cell lymphangiogenesis (Saarikangas et al., 2011; Yu et al., 2012). Thus, I-BAR domain proteins appear to directly link membrane

[1]Institute for Biophysical Chemistry, Hannover Medical School, Carl-Neuberg-Strasse 1, 30625 Hannover, Germany. [2]Gene Center and Department of Biochemistry at the Ludwig-Maximilians-University, Feodor-Lynen-Strasse 25, 81377 Munich, Germany. [3]Cellular Biotechnology, Institute of Biotechnology, PO Box 56, University of Helsinki, Helsinki 00014, Finland.
*These authors contributed equally to this work

‡Authors for correspondence (witte@genzentrum.lmu.de; faix.jan@mh-hannover.de)

Received 15 August 2013; Accepted 26 December 2013

Journal of Cell Science (2014) 127, 1279–1292 doi:10.1242/jcs.140756

deformation with actin polymerization in migration and cell morphogenesis.

To date, our knowledge of the function of I-BAR domain proteins comes largely from studies of the five mammalian orthologs, which are likely to have redundant functions. By contrast, the genome of the model organism *Dictyostelium discoideum* encodes one putative 357-residue I-BAR domain protein termed IBARa (Eichinger et al., 2005). A conserved domain search predicted that this protein had an N-terminal I-BAR domain and a C-terminal SH3 domain but no WH2-domain, thus conforming to the domain architecture of an IRSp53-like protein (Clarke et al., 2010). Because phylogenetic analysis revealed that IBARa from *D. discoideum* is rooted just before the branch point where IRSp53 and MIM-like subgroups of I-BAR domain proteins have evolved (Veltman et al., 2011), this ancestral protein is likely to display all the basic functions of this protein family. For this reason, here, we explored the functions of IBARa at the structural, biochemical and physiological level.

RESULTS

Structure and shape determination

To learn more about the structure and shape of the predicted I-BAR domain we crystallized the N-terminal fragment of *D. discoideum* IBARa (amino acids 1–259, termed here IBARa-N) and determined the 2.2-Å crystal structure by single-wavelength anomalous dispersion (SAD) on selenomethionine-substituted protein. Experimental phasing and density modification led to well-interpretable electron density for all four polypeptide chains (two dimers) of IBARa-N, with 323 water molecules and six non-solvent molecules in the asymmetric unit. The structure could be refined to an R value of 0.194 (R_{free}=0.230) with good stereochemistry (see Table 1).

IBARa-N is an almost entirely α-helical protein consisting of three antiparallel helices α1–α3, comprising residues 8–63, 68–142 and 147–221, respectively, followed by a shorter C-terminal helix α4 (amino acids 227–239, Fig. 1A). It autoassembles into a slightly bent homodimer with chains oriented opposite to another. The main helices α1–α3 of each monomer form a twisted ellipsoid with an interacting surface of ~3700 Å^2. The interface of the two interacting monomers is mostly hydrophobic (Fig. 1C; supplementary material Fig. S3), and the dimeric assembly has maximum dimensions of ~165 Å×25 Å×25 Å (Fig. 1A). The density of the loop region connecting α2 and α3 (residues ~140–155) was very weak, indicating that these loops are flexible and thus disordered in the crystal. In addition, the N-terminal eight residues of IBARa-N (plus the GPLGS overhang resulting from the GST fusion) and the C-terminal 20 residues were not traceable. Each of the four copies of IBARa-N in the unit cell has a slightly different start and end position for the weak-density areas (see supplementary material Fig. S1 for details) – the best-traceable electron density could be found for chain D and contains the residues 8–239. Fig. 1B shows the solvent-accessible electrostatic surface of IBARa-N in the same orientation as in Fig. 1A. IBARa-N is a highly charged protein (supplementary material Fig. S2), and it shows patches of positively charged areas on the convex side, which is necessary for membrane binding, but it also has a highly acidic patch in the middle of the concave side (mainly residues Glu-195, Glu-197 and Glu-199). Thus IBARa-N is showing a dipole structure as observed in other BAR domains. The obvious differences in positive charges on the convex side of the protein (Fig. 1B, bottom) result from the fact that each of the chains in the asymmetric unit shows slight differences in side-chain orientation and loop completeness. A symmetric-dimer model created from chain D only, by replacing chain C with a copy of chain D, shows a symmetric distribution of charges on the convex backbone area (supplementary material Fig. S4). A structural comparison of IBARa-N with IRSp53 (de Groot et al., 2011) showed that both proteins are highly similar [root-mean-square deviation (RMSD) 1.67 Å, Fig. 1D], and the comparison of IBARa-N with MIM (Millard et al., 2005; Lee et al., 2007) also underlines the structural similarity (supplementary material Fig. S5).

To analyze the structure of IBARa-N in solution, we performed small-angle X-ray experiments with the same construct as used in the crystallization setups. The shape of the scattering curve of IBARa-N already suggests an elongated shape of IBARa-N (e.g. Volkov and Svergun, 2003). The radius of gyration calculated from Guinier analysis (sR_g<1.3) of R_g=4.04 nm (supplementary material Fig. S6) is in good agreement with the theoretical R_g calculated from the crystal structure (R_g=3.96 nm), which lacks 33 residues present in the soluble construct owing to weak electron density (loop regions, N- and C-terminus). The theoretical scattering curve of the IBARa-N dimer was calculated with CRYSOL and it has the same shape as the measured data, confirming that the overall shape of the crystal structure is also present in solution (Fig. 1F). Moreover, we can rule out a monomeric state for the protein in solution (supplementary material Fig. S7). We then calculated independent sets of *ab initio* models from the SAXS data. All models were highly similar, and we were able to dock the crystallographic dimer into the final averaged and filtered *ab initio* shape with a good fit

Table 1. Data collection and refinement statistics

	Se-IBARa (amino acids 1–259)
Data collection	
Wavelength (Å)	0.9796
Spacegroup	$P2_1$
Cell dimensions	
a,b,c (Å)	59.1, 60.2, 147.6
α,β,γ (deg)	90.0, 100.4, 90.0
Resolution (Å)	50-2.21 (2.26-2.21)[a]
R_{merge} (%)	7.2 (61.2)[a]
$I/\sigma I$	10.21 (1.88)[a]
Completeness (%)	98.5 (85.3)[a]
Redundancy	3.19 (2.49)[a]
Refinement	
Resolution	48.4-2.21
No. of reflections	99167
R_{work}/R_{free}	19.4/23.0
No. of atoms	7559
Protein	7254
Ligands	29
Water	276
B-factors	
Protein	53.8
Ligands	68.2
Water	49.0
RMSD	
Bond lengths (Å)	0.004
Bond angles (deg)	0.766
Ramachandran (%)	
Favorite	97.9
Allowed	2.1
Outliers	0
PDB Accession Code	4NQI

[a]Values in parentheses are for highest resolution shell.

Journal of Cell Science (2014) 127, 1279–1292 doi:10.1242/jcs.140756

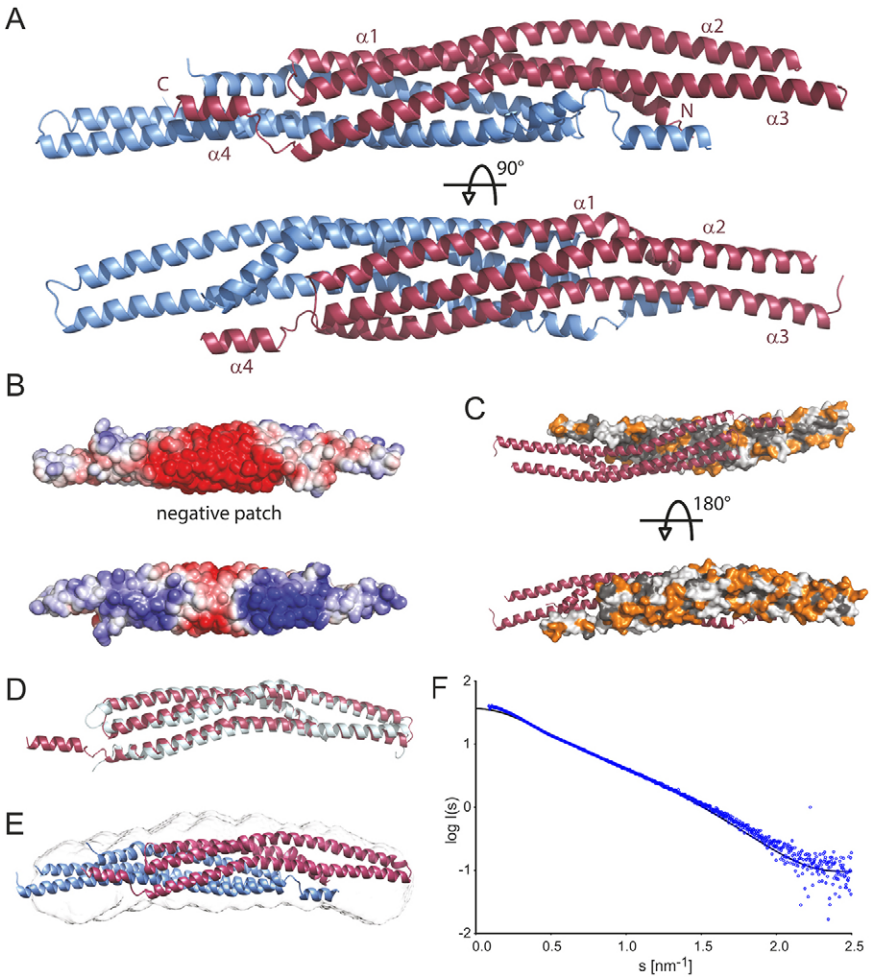

Fig. 1. Structure of IBARa. (A) The structure of the IBARa-N dimer is shown as a ribbon representation in two orientations. The helices α1–α4 are labeled. One chain of the dimer is shown in red and the other is shown in blue. (B) The solvent-accessible electrostatic surface (red, −5 *kT*/e; blue, +5 *kT*/e), calculated with APBS (Baker et al., 2001), shows a positively charged surface on the convex 'backbone' of the dimer and a negatively charged patch on the concave side. (C) Dimerization of IBARa-N. The figure shows the contact surface area of one monomer (hydrophobic residues are dark gray, charged residues are orange), with the second monomer shown as a cartoon model (red). The dimerization is mainly driven by hydrophobic interactions between the two monomers. In comparison, the outside of the dimer shows a more balanced distribution of hydrophobic and charged residues. (D) Superposition of one chain of IBARa-N (red) and one chain of IRSp53 (white, PDB code, 2YKT) shows a high structural similarity between the two proteins (RMSD 1.67 Å). (E) The final volume of IBARa-N in solution obtained by *ab initio* modeling from SAXS data with docked crystallographic IBARa-N dimer shows a good fit. Please note that the curvature of the proteins seems to be slightly more pronounced in solution. (F) The theoretical scattering curve of IBARa-N, calculated with CRYSOL, and the measured data support the idea that the shape of IBARa-N is highly similar in crystal form and in solution.

(Fig. 1E). The *ab initio* models of IBARa-N show a slightly more pronounced curvature, in good agreement with our data showing that IBARa-N can evaginate and bend membranes. Because the structure of IBARa-N shows the typical twisted ellipsoid α-helical arrangement, previously found in inverse BAR domains (Saarikangas et al., 2010), we next analyzed the lipid binding and bending properties of IBARa-N.

IBARa binds and evaginates PIP_2-containing membranes

Previous studies have established that I-BAR domains interact with phospholipid-rich membranes through positively charged patches located at the distal ends of the I-BAR domain (Suetsugu et al., 2006a; Mattila et al., 2007; Saarikangas et al., 2008; Pykäläinen et al., 2011). The specificity of IBARa binding to a variety of phospholipids was assessed by cosedimentation assays using liposomes of different lipid compositions. IBARa-N bound to a variety of phospholipids, with a preference for phosphoinositides. Based on a cosedimentation assay carried out with different phosphoinositides, I-BARa-N appeared to display highest affinity towards phosphatidylinositol (4,5)-bisphosphate [$PI(4,5)P_2$] (Fig. 2A,B). To analyze and quantify the $PI(4,5)P_2$-clustering activity of IBARa-N, the self-quenching of BODIPY-TMR–$PI(4,5)P_2$ fluorescence, which results from clustering, was monitored upon addition of the protein. Addition of IBARa-N resulted in self-quenching of the fluorescent probe molecules (Fig. 2C). The signals were plotted to obtain values for $PI(4,5)P_2$ clustering at different concentrations of protein. These data suggest that the positively charged 'lipid-binding interface' at the N-terminus of the I-BAR domain of IBARa can mediate efficient clustering of $PI(4,5)P_2$. The rotational diffusion of the fatty acyl chains was evaluated by fluorescence anisotropy, with DPH as a probe. This is a rod-like highly hydrophobic molecule that intercalates into the hydrophobic core of a lipid bilayer without affecting the physical properties of the membranes, and can thus be used for monitoring changes in the trans-gauche isomerization of phospholipid acyl chains in the membrane interior (Zaritsky et al., 1985). Anisotropy changes were interpreted here in terms of fluidity or variation in microviscosity. As a control, the binding of the MIM I-BAR domain to $PI(4,5)P_2$-containing membranes induced a significant increase in DPH anisotropy because the N-terminal amphipathic α-helix inserts into the acyl-chain region of the bilayer and therefore modulates its microviscosity (Saarikangas et al., 2009). Notably, IBARa-N had no significant effect on DPH anisotropy, strongly suggesting that this I-BAR domain does not insert into the acyl-chain region of the bilayer (Fig. 2D). This is consistent with the X-ray structure, which does not show any N-terminal amphipathic α-helices that could insert into membranes (see Fig. 1).

Because the 'zeppelin-like' shape and structure of IBARa means that the protein is a member of the subfamily of inverse BAR domain proteins, we analyzed its lipid-bending mode using large unilamellar vesicles (LUVs). The addition of 5 µM IBARa-N to a LUV solution with a total lipid concentration of 200 µM

Journal of Cell Science (2014) 127, 1279–1292 doi:10.1242/jcs.140756

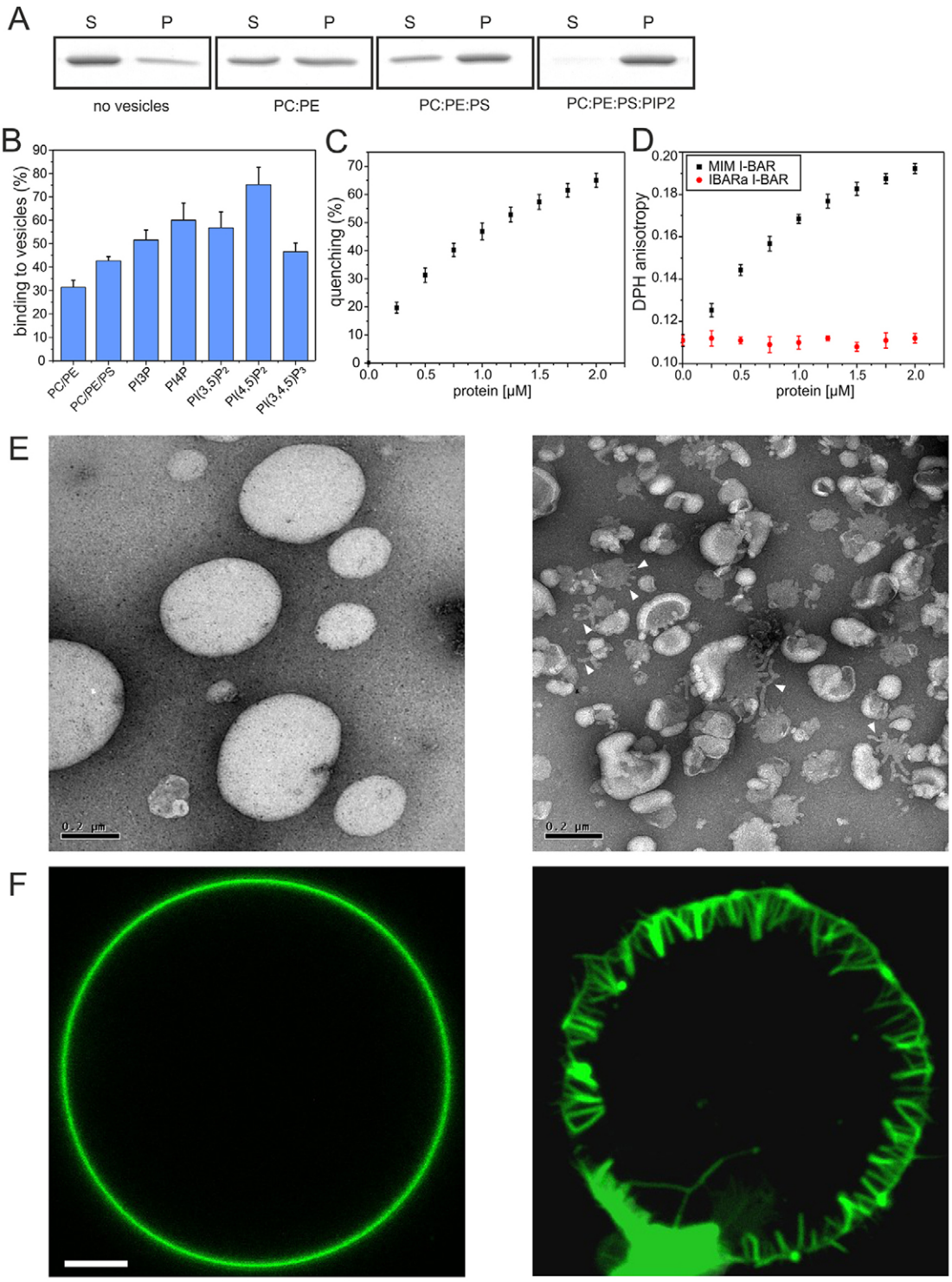

Fig. 2. The *Dictyostelium* I-BAR domain binds to and tubulates phosphoinositide-containing vesicles. (A) Proteins cosedimented with vesicles were present in the pellet fraction (P) and unbound free proteins were detected in the supernatant (S) by SDS-PAGE and Coomassie Blue staining. (B) Quantification of membrane-bound IBARa-N in the presence of vesicles with different lipid compositions. The final concentrations of the protein and lipids were 3 μM and 1 mM, respectively. Lipid compositions were POPC:POPE at a ratio of 8:2, POPC:POPE:POPS at a ratio of 6:2:2 and POPC:POPE:POPS:PIP_x at a ratio of 5:2:2:1. (C) Quenching of BODIPY-FL–$PI(4,5)P_2$ demonstrated that IBARa-N sequesters $PI(4,5)P_2$ at the membrane. (D) The *Dictyostelium* I-BAR domain does not affect steady-state DPH anisotropy. This suggests that the lipid binding of this protein does not influence membrane fluidity. (E) Transmission electron microscopy analysis of large unilamellar vesicles containing 10% $PI(4,5)P_2$, incubated with IBARa-N showing that the *Dictyostelium* I-BAR domain causes tubulation of PIP_2-containing membranes (right). Control vesicles in the absence of protein are shown to the left. The membrane morphology of vesicles was visualized by negative staining. The lipid composition was POPC:POPE:POPS:PIP_2 at a ratio of 50:20:20:10 and the final concentrations of protein and lipids were 5 μM and 200 μM, respectively. Arrowheads show elongated membrane tubules. Scale bar: 0.2 μm. (F) Control giant unilamellar vesicle in the absence of protein (left). 1 μM of I-BARa-N induced membrane invaginations of giant unilamellar vesicles (right). The lipid composition was POPC:POPE:POPS:PIP_2:TopFluor-PIP_2 (50:20:20:9:1). Scale bar: 5 μm.

Journal of Cell Science

Journal of Cell Science (2014) 127, 1279–1292 doi:10.1242/jcs.140756

was sufficient to cause marked fragmentation of the LUVs (Fig. 2E). From this experiment, it became obvious that IBARa-N was also able to initiate and elongate membrane tubules (Fig. 2E, white arrowheads). To assess whether IBARa-N drives the formation of either positive or negative membrane curvature, the protein was incubated together with pre-formed fluorescently labeled giant unilamellar vesicles (GUV) and analyzed by fluorescence microscopy. After addition of 1 µM IBARa-N to the GUVs, invaginations of the membrane were observed, demonstrating that IBARa generates negative membrane curvature (Fig. 2F). Of note, in the absence of PI(4,5)P_2 no tubulation of the membrane was observed (data not shown).

Localization of endogenous IBARa

To analyze the subcellular localization and dynamics of IBARa, we generated N- and C-terminal fusions with GFP. However, *Dictyostelium* cells transfected with these constructs displayed only diffuse signals, suggesting that the fusions with GFP are not functional. To corroborate this notion, we raised specific polyclonal antibodies against a C-terminal IBARa fragment (amino acids 225–357). After affinity purification, the antibody was used to analyze the localization of the endogenous protein by indirect immunofluorescence microscopy. Interestingly, IBARa prominently localized at large vacuolar structures that were interconnected by a tubular network (Fig. 3A; supplementary material Movie 1, Fig. S8) – presumably the contractile vacuole (CV), which is an osmoregulatory organelle (Gabriel et al., 1999). To confirm this, fixed cells were additionally stained for endosomes, as well as for the CV marker csA-Rh50, after ectopic expression of this construct in wild-type (WT) cells (Mercanti et al., 2006). As shown in Fig. 3A, IBARa localization was clearly distinct from p80-stained endosomes but the protein perfectly

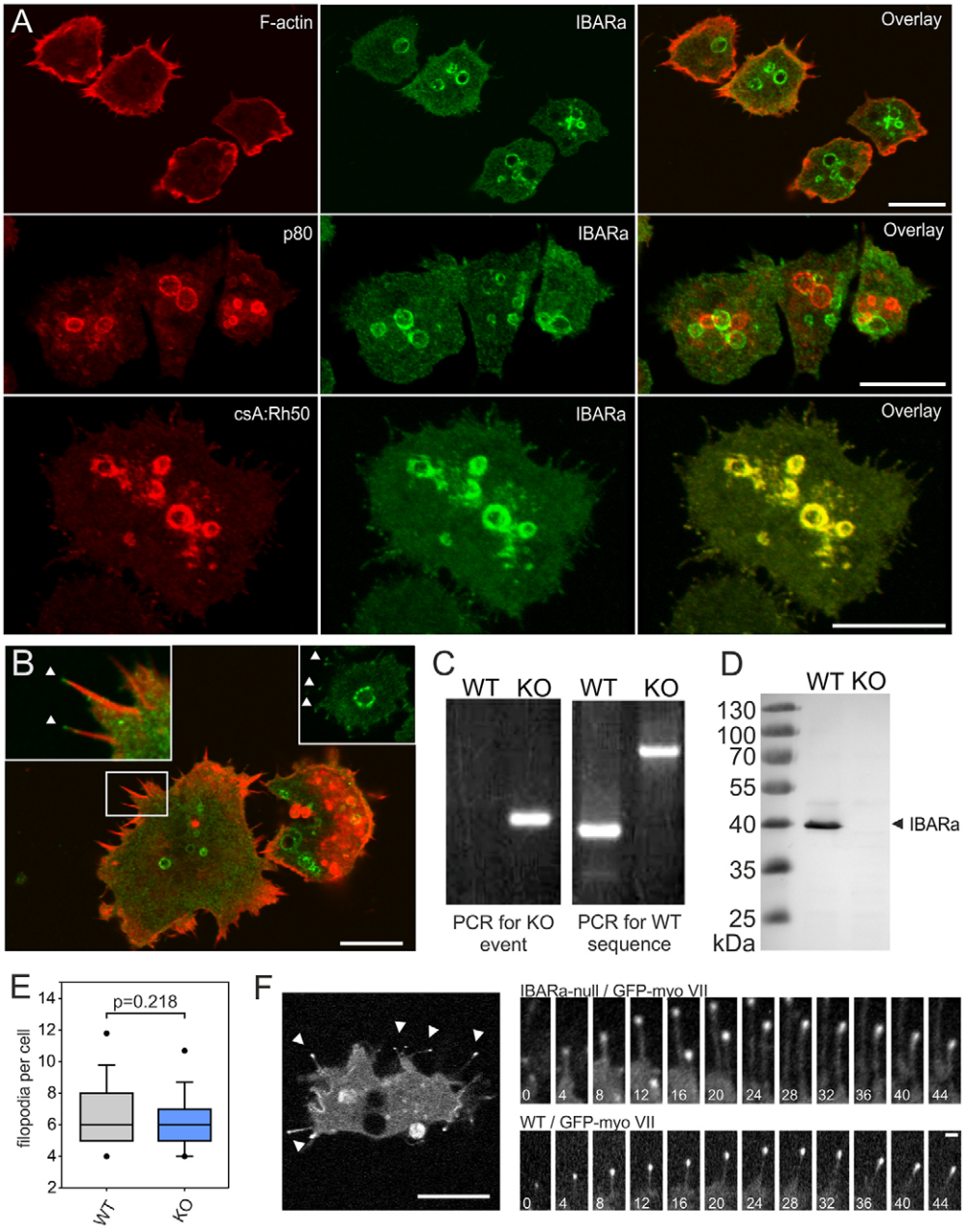

Fig. 3. Endogenous IBARa localizes to CVs and the tips of filopodia. (A) Confocal images of cells stained for IBARa and F-actin (stained with fluorescently labeled phalloidin) (top panel), IBARa and endosomes (middle panel) or IBARa and the CV marker csA-Rho50 (lower panel). (B) Endogenous IBARa also localizes to the distal tips of filopodia (white arrowheads). The magnified inset in the upper-left corner shows IBARa (green) at the tips of filopodial F-actin bundles (red), and the inset in the upper-right corner shows IBARa at filopodial tips without the phalloidin staining to better illustrate the accumulation of the protein in the tips. (C) Generation of the IBARa-null mutant by gene disruption. Genetic knockout (KO) of the *ibrA*-gene was confirmed by two PCRs to screen for disruption (left panel) or the presence of the WT allele (right panel) using specific primer pairs. (D) The absence of IBARa in the mutant was confirmed by western blotting using anti-IBARa antibodies. (E) The number of filopodia per cell is not altered in the IBARa-null mutant. The average number of filopodia for WT and IBARa-null cells was determined from phase-contrast time-lapse movies, which allowed discrimination between retraction fibers and filopodia. There was no statistically significant difference ($P=0.218$). The box boundaries represent the upper and lower quartile, the whiskers show the upper and lower percentile and the median is shown as a line. (F) WT and IBARa-null cells were transfected with GFP–myosin-VII, as a marker for canonical filopodia, and were subjected to time-lapse imaging using confocal microscopy to score protruding and retracting filopodia. Tip localization of GFP–myosin-VII in a representative IBARa-null cell is shown in the left panel (white arrowheads). Time is shown in seconds. Scale bars: 10 µm (A, B and F, left), 1 µm (F, right).

Journal of Cell Science

Journal of Cell Science (2014) 127, 1279–1292 doi:10.1242/jcs.140756

colocalized with csA-Rh50, corroborating its presence on the CV system. Additionally, IBARa was seen at the distal tips of filopodia (Fig. 3B). In summary, this showed that IBARa is associated with dynamic regions in membranes and suggested that the protein is involved in osmoregulation and filopodia formation.

Generation and analysis of IBARa-null mutants

To assess the contribution of IBARa to these processes, the *ibrA* gene was disrupted by homologous recombination. The inactivation of the *ibrA* gene was validated by PCR using specific primers (Fig. 3C), and the absence of IBARa protein was additionally confirmed by western blotting (Fig. 3D). Owing to its localization in filopodia tips and the possible involvement of the I-BAR protein IRSp53 in filopodia formation (Millard et al., 2005; Vaggi et al., 2011), we quantified the total number of filopodia in randomly migrating IBARa-null and WT cells using phase-contrast microscopy. However, and consistent with a recent report (Veltman et al., 2011), we could not find a significant difference; both cell lines formed about six filopodia on average (Fig. 3E). Additionally, we monitored the protrusion and retraction of filopodia in WT and mutant cells expressing the filopodial-tip-marker protein GFP–myosin-VII (Tuxworth et al., 2001). Again, no differences between WT and mutant cells were observed; in both cell lines filopodia protruded with a speed of ~0.4 µm/s (Fig. 3F). Taken together, these findings suggest that IBARa is not essential for filopodia formation.

The IBARa-null mutant displays substantial defects in osmoregulation

Because endogenous IBARa most prominently decorates the CV (Fig. 3A), next we quantified the numbers of this organelle in WT and mutant cells using the live-cell dye FM2-10 (Heath and Insall, 2008). Analysis by confocal microscopy revealed that, in the absence of IBARa, the cells displayed a significantly increased number of CVs as compared to control (Fig. 4A,B), indicating that there is a functional defect of this osmoregulatory organelle, either in filling, discharge or fusion with the plasma membrane. To monitor the dynamics and discharge of the CVs in WT and mutant cells, ectopically expressed GFP–Dajumin was used as a CV marker suitable for live-cell imaging. This probe was previously reported to label entire CVs, but not to stain the endosomal compartment (Gabriel et al., 1999). First, we tested whether the CVs of the null-mutant cells were still able to expel liquid. To do this, the cells were incubated in low osmolarity phosphate buffer to stimulate CV activity. This buffer was supplemented with the soluble fluorescent dye tetramethylrhodamine (TAMRA). Confocal time-lapse imaging revealed that the mutant cells were still able to fill and discharge their CVs, albeit at an apparently reduced rate when compared to WT cells (Fig. 4C; supplementary material Movie 2). Notably, with the beginning of the CV discharge there was an influx of exterior liquid, as visualized by diffusion-driven incorporation of TAMRA into the compartment, demonstrating the formation of unspecific channels or pores when the CV fuses with the plasma membrane (Fig. 4C, white arrowheads). Of note, there was a broader cellular distribution of the GFP–Dajumin probe in these experiments as compared to the CV structures that were labeled by IBARa antibodies. To correlate the localization of both probes, the GFP–Dajumin-expressing WT cells were immunostained with anti-IBARa antibodies (Fig. 4D). Confocal microscopy showed that IBARa and GFP–Dajumin colocalize at CVs; however, GFP–Dajumin was also seen on other structures (for instance, around the nucleus) presumably comprising the ER.

Next, we compared the survival rate of IBARa-null and WT cells by incubation under hypotonic conditions for different time periods. This assay revealed that after 5 h in water >40% of the IBARa-null cells had died, whereas the number of viable WT cells remained almost constant, indicating that the absence of IBARa causes a strong defect in osmoregulation (Fig. 4E). To quantify this defect in more detail and in the least invasive way, we used high-speed phase-contrast imaging to visualize WT and mutant cells that were moderately flattened by an overlaying thin agar sheet. Interestingly, ~10% of all IBARa-null cells failed to form or maintain a CV after transfer into hypotonic buffer, and subsequently lysed (Fig. 4F, upper panel; supplementary material Movie 3). These cells were morphologically distinct from the others, as shown by their grainy cytoplasm and a swollen and round appearance. Unexpectedly, upon contact, they also became detectable as potential prey for neighboring IBARa-null cells that contained CVs (Fig. 4F, lower panel; supplementary material Movie 4), suggesting that there is a marked alteration in the cell-surface properties of these cells. The majority of IBARa-null cells still formed functional CVs; however, these were larger in size and displayed a discharge rate that was reduced by 23% as compared to the CVs of WT cells (Fig. 4G). Taken together these findings establish IBARa as a crucial factor in CV function.

IBARa affects growth, adhesion and phagocytosis

Because defects in the CV system of *Dictyostelium* cells are frequently associated with defects in growth or cytokinesis (Kwak et al., 1999; Gerald et al., 2002; Damer et al., 2005; Damer et al., 2007), we compared the growth of WT and mutant cells in bacterial lawns on agar plates as well as in shaken suspension (Fig. 5A,B). In both conditions, the growth of the null mutant was markedly slower than that of WT cells. In shaken suspension, the null mutant reached a density of only $\sim 8\times10^6$ cells/ml, whereas the growth of the WT became stationary at $>1.3\times10^7$ cells/ml. Taken together, these findings suggest defects in cytokinesis, endocytosis or adhesion, either alone or in combination.

Next, we therefore compared the efficiency of uptake of the fluid-phase marker TRITC–Dextran in WT and IBARa-null cells. However, no defects in macropinocytosis between WT and mutant cells were measurable in our assays (Fig. 5C). Then we compared the efficiency of phagocytosis in WT and IBARa-null cells. Phagocytic activity was measured by the uptake of fluorescently labeled yeast particles (FLY), as well as nocodazole-treated, fluorescently labeled dumbbell-shaped yeast particles (NTY). We observed an impaired uptake of both types of particles by the null mutant (Fig. 5D) and, as expected, the ingestion of NTY was less efficient than that of the spherical FLY particles. In line with these findings, IBARa was detected at the rim of constricting phagocytic cups (Fig. 5E; supplementary material Movie 5). Thus, in endocytosis, IBARa contributes predominantly to phagocytosis.

Because numerous cellular processes require an adaptation of the cell morphology, which can be linked to substantial changes in volume (for instance, during cytokinesis), we analyzed the dynamics of cell-shape changes by time-dependent measuring of the adhesion area using reflection interference contrast microscopy (RICM). WT cells showed highly dynamic contracting and spreading behavior, resulting in a highly fluctuating cell adhesion area (Fig. 5F; 5G, upper panel). By contrast, IBARa-null cells remained relatively static (Fig. 5F; 5G, lower panel). Interestingly, the median size of the adhesion area in WT and null-mutants did not differ significantly (Fig. 5F), whereas the

Journal of Cell Science (2014) 127, 1279–1292 doi:10.1242/jcs.140756

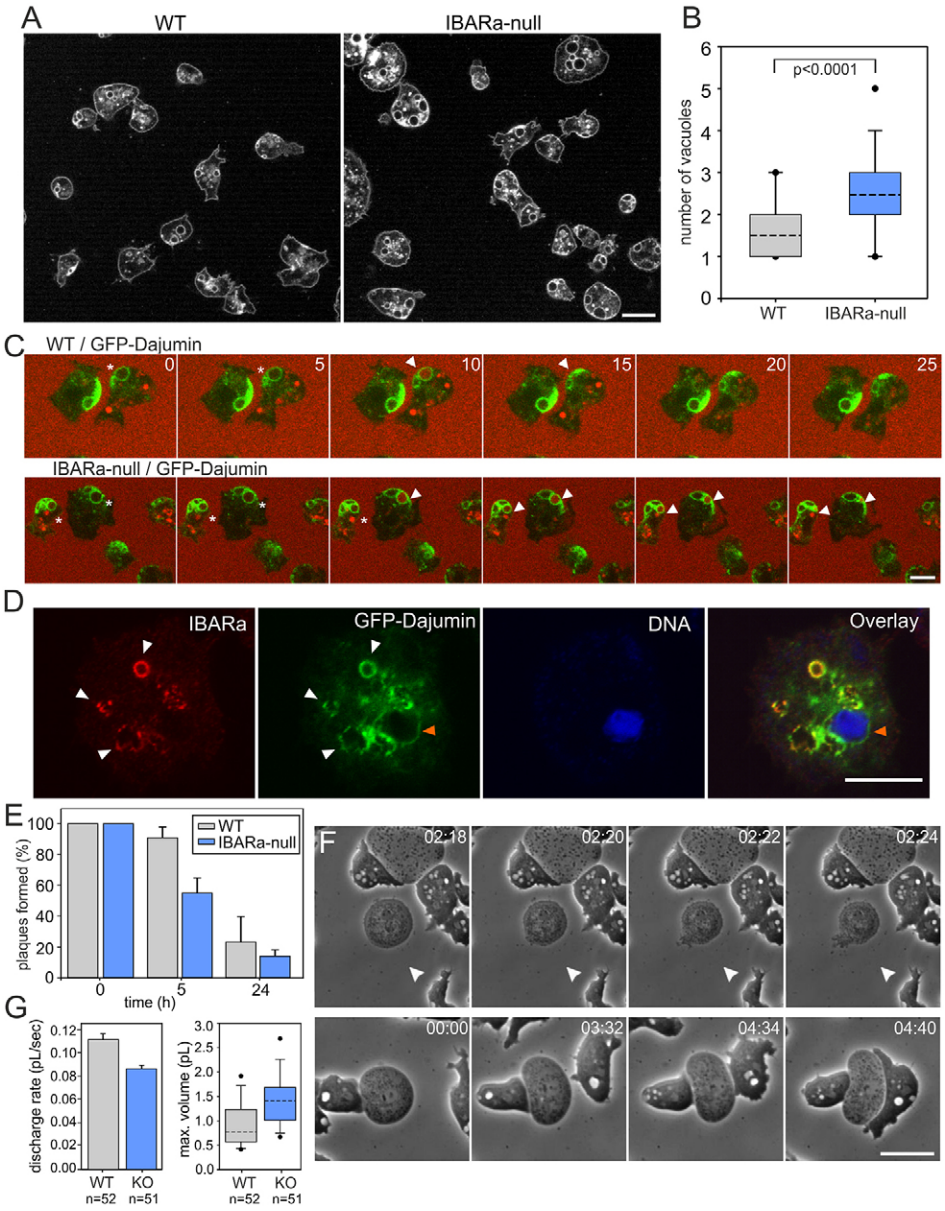

Fig. 4. Impaired CV function in IBARa-null mutants. (A) The morphology of CVs in WT and IBARa-null cells visualized by the lipophilic dye FM2-10. (B) The null-mutant showed a significantly increased number of vacuoles. The box boundaries represent the upper and lower quartile, the whiskers show the upper and lower percentile and the median is shown as a dashed line. The difference is statistically significant ($P<0.0001$). (C) The CVs of IBARa-null mutant cells were still able to expel their content. Loaded CVs in WT and IBARa-null cells attached to the membrane prior to their discharge (white asterisks), and subsequently the entry of TAMRA into the CV was observed (white arrowheads). Confocal sections of the vacuolar network visualized by GFP–Dajumin are shown. Time is shown in seconds. (D) GFP–Dajumin labels the CV (white arrowheads) and other membranous compartments such as the ER (orange arrowheads). GFP–Dajumin-expressing cells were fixed and labeled with anti-IBARa polyclonal antibodies (red), GFP nanobodies (green) and TO-PRO-3, to visualize the nucleus (blue). (E) IBARa-null mutants are more sensitive to hypotonic stress. Considerably fewer mutant cells than WT cells survived incubation in water after 5 or 24 h. Results show the mean±s.e.m., $n=4$. (F) Phase-contrast imaging of IBARa-null cells in low osmolarity PB buffer overlaid with a thin sheet of agar (top panel). White arrowheads indicate a cell lacking a CV, which lysed under these conditions. Lower panel, autophagy of IBARa-null cells devoid of CVs by CV-containing cells upon establishing contact. Time is shown in minutes and seconds. (G) Left, the CV discharge rate of WT and IBARa-null cells in PB buffer. Right, the maximal volume distribution of tracked vacuoles prior to discharge in picoliters, shown by box plot representation. Scale bars: 10 µm.

time-resolved distribution of the measured areas was markedly broader in the WT as opposed to the mutant (Fig. 5F). These data do not support a general defect in adhesion, but rather suggest a defect in adaption of the cellular volume in response to morphological changes.

IBARa is required for normal cytokinesis

Previous work has revealed that constriction of the cleavage furrow is accompanied by a drastic efflux of water as shown by highly active CV formation during cytokinesis (Fukui and Inoué, 1991). Therefore, we analyzed dividing WT and mutant cells by phase-contrast time-lapse microscopy. We found that IBARa-null cells were frequently unable to finish separation into daughter cells (Fig. 6A). In contrast to the WT, which divides by symmetric constriction, the mutant frequently began to separate into four or more daughter cells at the beginning of anaphase. Some of them, however, failed to separate completely and reunited into the same cell body, resulting in fewer daughter cells owing to this asymmetric cell division (supplementary material Movies 6, 7). To substantiate this defect in cytokinesis, we quantified the number of nuclei after DAPI staining in cells grown on plates or in shaken suspension (Fig. 6B,C). In both conditions, IBARa-null cells became highly multinucleated and, as expected, the cytokinesis defect was more pronounced in cells grown in shaken suspension, during which the cells lack adhesion to the substratum and are exposed to strong shear forces. In the latter case, 38% of IBARa-null cells contained three or more nuclei, whereas this value was <3% in the WT (Fig. 6C). Finally, we explored the subcellular localization of IBARa in dividing myosin-II-null cells, because in adherent culture these cells divide by regular cytokinesis in a manner comparable to the WT (Neujahr et al., 1997). However, owing to their increased adhesion to the substrate, a much larger fraction of cells can be captured in various stages of cytokinesis (Weber et al., 1999). During mitosis, the CV system was much more dispersed into smaller vesicles when compared to its morphology in interphase cells, as assessed by immunolabeling with IBARa antibodies. We observed only an occasional enrichment of IBARa-containing

Journal of Cell Science (2014) 127, 1279–1292 doi:10.1242/jcs.140756

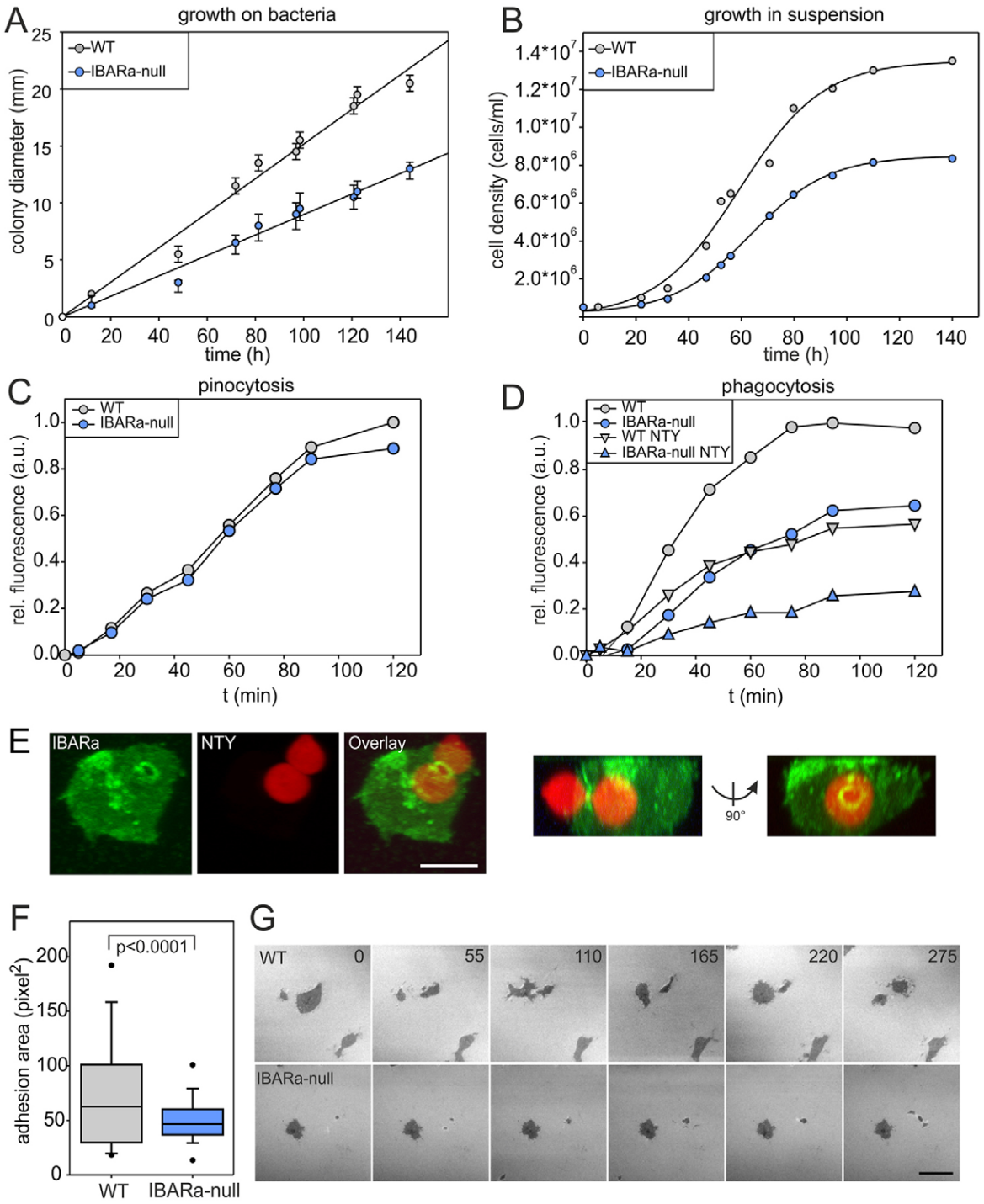

Fig. 5. IBARa-null cells show defects in growth, adhesion and phagocytosis. (A,B) Reduced growth rates of IBARa-null cells. (A) IBARa-null cells formed considerably smaller colonies on bacterial lawns when compared to WT cells, indicating a substantial growth defect. For each cell line, the results show the mean±s.e.m., $n=4$. (B) Reduced growth was also observed in shaken suspension culture. (C) Pinocytosis was not affected in the absence of IBARa. Fluid-phase uptake was measured by the addition of fluorescent dextran (10 μg/ml) to the nutrient medium. (D) Phagocytosis was strongly impaired in IBARa-null mutants. Uptake of FLY particles by WT (gray) and mutant (blue) cells was assayed in shaken suspension in growth medium. The uptake of either untreated (circles) or nocodazole-treated dumbbell-shaped yeast cells (NTY, triangles) was strongly reduced in the null mutant, when compared to control. a.u., arbitrary units. (E) IBARa was found at the rim of constricting phagocytic cups. 3D reconstructions from confocal sections are shown. (F,G) Reduced dynamics of cell spreading and contraction in IBARa-null mutants. (F) WT and mutant cells display a similar median adhesion area. The box plot representation of time-resolved measured values shows a broadly spread distribution of the contact areas for the WT, whereas the values for mutant cells accumulated in a narrow range. The size of the contact area for each cell was determined every 8 s for an 8-min period. The box boundaries represents the 25th and 75th percentile, the whiskers the 10th and 90th percentile and dots represent maximum and minimum values. (G) WT cells behaved highly dynamic by continuously contracting and spreading their cell bodies on a glass surface as compared to IBARa-null cells, which were considerably less dynamic. Time-lapse recordings of the contact areas were obtained by reflection interference contrast microscopy (RICM). Note the substantial changes in the adhesion area of WT cells, whereas IBARa-null mutants appear to be more static. Time is shown in seconds. Scale bars: 10 μm.

Journal of Cell Science (2014) 127, 1279–1292 doi:10.1242/jcs.140756

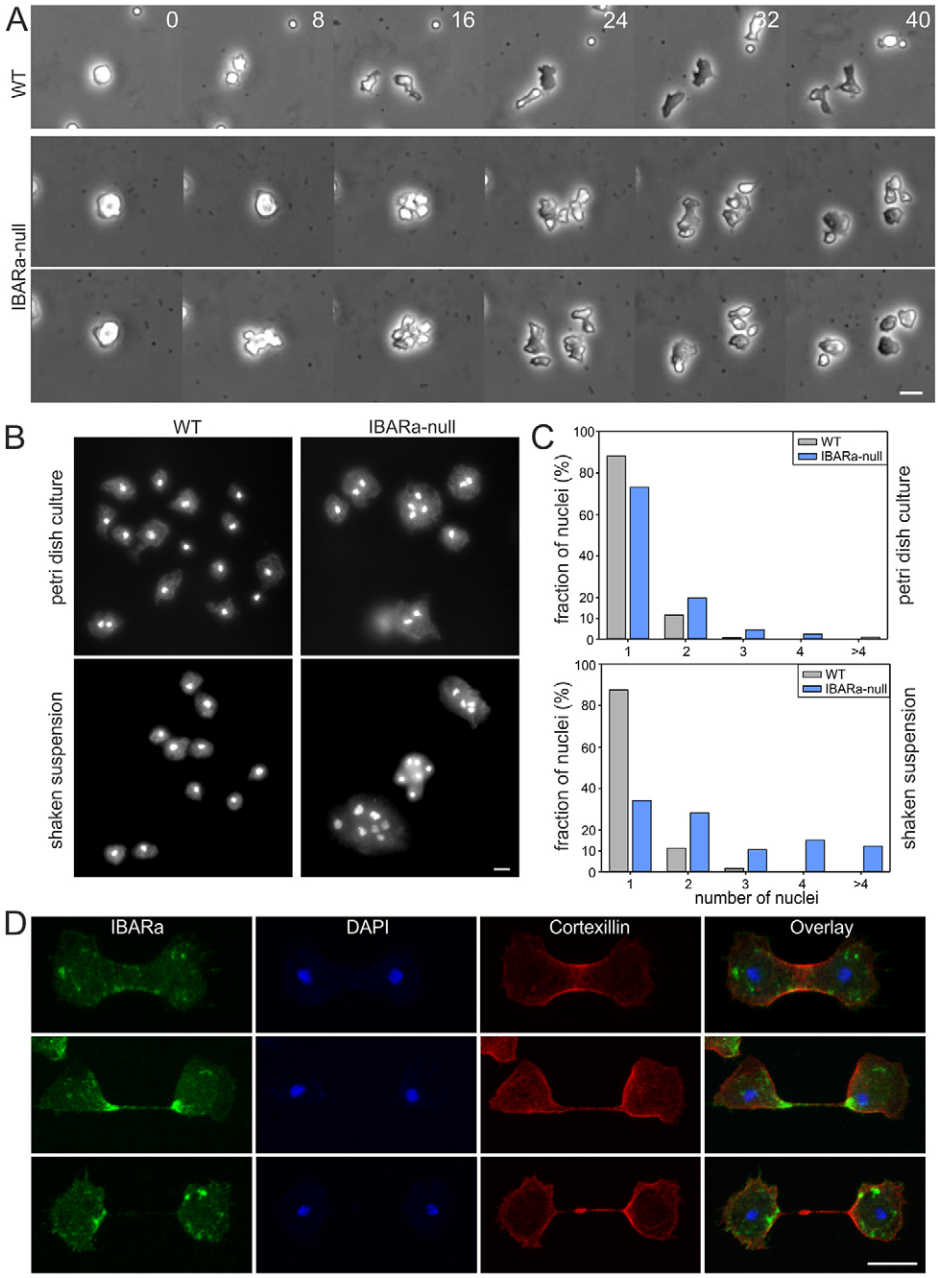

Fig. 6. IBARa-null cells display a marked defect in cytokinesis. (A) In contrast to WT cells, which regularly divide into two daughter cells (upper gallery), multinucleated mutant cells frequently broke up into multiple fragments, some of which reunited again into a single cell (middle and lower galleries). Time series produced using phase-contrast microscopy of mitotic cells (beginning at anaphase) are shown. Time is given in seconds. (B) In WT and mutant cells cultivated with nutrient medium, either on Petri dishes or in shaken suspension, the nuclei were stained with DAPI to visualize mono- and multi-nucleate cells. (C) A histogram showing the distribution of the number of nuclei in WT cells and IBARa-null cells. Over 700 nuclei were counted for each strain. (D) IBARa localization in dividing myosin-II-null cells. Top panel, during early telophase IBARa-containing vesicles (green) accumulated occasionally in the cleavage-furrow region of dividing myosin-II-null cells. The cleavage furrow marker protein cortexillin (red) was employed to score mitotic cells (Weber et al., 1999) and the nuclei were stained with TO-PRO-3. Middle panel, in the final stages of cytokinesis, IBARa became transiently enriched in small foci connecting the separating daughter cells. Lower panel, in about 50% of the cells, IBARa was seen only in one of the daughter cells. Scale bars: 10 μm.

vesicles in the vicinity of the cleavage-furrow region stained by the actin-bundling protein cortexillin during telophase (Weber et al., 1999). Most strikingly, however, during the final stages of cytokinesis, IBARa became highly enriched in foci connecting the separating daughter cells (Fig. 6D; supplementary material Movies 8–10). These findings strongly suggest that IBARa actively contributes to membrane remodeling during mitotic cell division.

DISCUSSION

The X-ray structure of *D. discoideum* IBARa-N shows high similarity to the existing structures of I-BAR domain proteins like IRSp53 (de Groot et al., 2011) and MIM (Lee et al., 2007). Two IBARa-N monomers autoassemble into an antiparallel dimer forming the typical I-BAR architecture, which has only a small angle of ~10° between the monomers (in comparison to the more bent structures of F- or N-BAR domains) (Frost et al., 2009). Small-angle X-ray scattering data show that the conformation of IBARa-N observed in the crystal structure is also present in solution, and at the same time rule out the existence of significant amounts of monomers. The dipole structure orients IBARa-N at the membrane through electrostatic interactions of the positive side with the phospholipids and repulsive effects of the negatively charged opposite side. Because we could not identify any regions that are potentially inserted into the membrane, for instance as seen with the N-terminal amphipathic helix in MIM (Saarikangas et al., 2009), IBARa-N presumably binds to membranes exclusively by electrostatic interaction with negatively charged $PI(4,5)P_2$, thereby inducing membrane deformation in a manner similar to IRSp53 (Mattila et al., 2007). This mode of membrane interaction is also supported by the fluorescence anisotropy experiments using DPH-labeled lipids, in which IBARa shows no effect on anisotropy, similar to IRSp53 (Saarikangas et al., 2009) but in stark contrast to MIM, which causes increased anisotropy owing to its insertion into the membrane (Saarikangas et al.,

Journal of Cell Science (2014) 127, 1279–1292 doi:10.1242/jcs.140756

2009). As a consequence, the opposite side of IBARa-N is oriented towards the cytosol, with the negatively charged patch in the middle of the IBARa-N concave side being accessible for potential protein–protein interactions. As previously reported for other proteins (Mercanti et al., 2006), the acidic patch might also serve as a localization signal to the CV.

Localization of IBARa

The great advantage of analyzing GFP fusion proteins is that they provide the capability of following the dynamics of the proteins by live-cell imaging to provide understanding of their cellular function. This approach has recently been used to analyze the function of IBARa in phagocytosis and clathrin-coated pinocytosis (Clarke et al., 2010; Veltman et al., 2011). However, with the exception of a moderate enrichment of IBARa in constricting phagocytic cups (Clarke et al., 2010) and endocytic vesicles (Veltman et al., 2011), a distinct cellular localization of IBARa was not seen. In our hands, both N-terminal and C-terminal GFP fusions with IBARa were more or less uniformly distributed in the cytoplasm, even when the proteins were expressed at low levels, suggesting, that in this case, fusions with GFP are not functional. This notion was further confirmed by immunolabeling of the endogenous IBARa protein in fixed cells, which showed that IBARa accumulated in the membrane of the CV, in filopodia and in constricting phagosomes. Thus, the only localization of IBARa seen with both antibody labeling and expression of the GFP fusion protein was at constricting phagosomes enclosing dumbbell-shaped NTY particles. What could be the reason for this? We hypothesize that owing to the atypical form of the NTYs, the *Dictyostelium* cells attempt to close the phagocytic cup after engulfing the first half of the NTY. However, because this fails owing to presence of the neck region of the NTY, the cells appear to respond by localizing excess IBARa protein to this region. This notion is also consistent with massive accumulation of coronin in the constricting phagosomes of *Dictyostelium* cells engulfing NTYs, as assessed by immunolabeling or by the expression of GFP–coronin (data not shown). Therefore, even a poorly functional GFP–IBARa fusion construct might yield a detectable signal in this case.

IBARa is dispensable for filopodium formation

The localization of IBARa in the distal tips of filopodia, its domain architecture and our finding that IBARa is able to generate negative curvature to evaginate membranes together suggest that the protein carries out an IRSp53-like function in filopodium formation in *Dictyostelium* cells (Krugmann et al., 2001; Millard et al., 2005; Mattila et al., 2007). However, and consistent with recent work (Veltman et al., 2011), inactivation of IBARa did not abolish the formation of filopodia. Thus, this protein is either not essential and carries out only modulatory functions in this process, or other membrane-sculpting proteins execute overlapping functions with IBARa in the formation of filopodia. Of note, although F-BAR-containing proteins are expected to participate in the induction of invaginations, in mammalian cells two F-BAR proteins, srGAP/MEGAP and PACSIN/syndapin, have been reported to induce filopodia-like membrane protrusions (Wasiak et al., 2001; Guerrier et al., 2009; Carlson et al., 2011). The *Dictyostelium* genome encodes six F-BAR proteins, including four MEGAPs and one syndapin-like protein, of which only MEGAP1 and MEGAP2 have been characterized. These two proteins have been shown to be implicated in cell motility and tubulation of the CV system (Eichinger et al., 2005; Heath and Insall, 2008). Thus, it remains to be seen whether some of the remaining F-BAR proteins contribute to filopodium formation.

IBARa function in cytokinesis

Why is IBARa, residing most prominently on the CV (see below), involved in other processes such as cytokinesis? A microscopic analysis of cytokinesis in *Dictyostelium* cells has previously revealed that the constriction of the cleavage furrow is accompanied by an efflux of water, as evidenced by highly active CV formation during cytokinesis (Fukui and Inoué, 1991). This implies an important function for the CV system in *Dictyostelium* cytokinesis and might explain the phenotypic defects reported for genetic knockout mutants lacking the CV constituents CpnA and LvsA (Kwak et al., 1999; Gerald et al., 2002; Damer et al., 2007). This function is also consistent with the substantial defect of IBARa-null cells in mitotic cell division, because these cells display impaired removal of water, as evidenced by their sensitivity to incubation in hypotonic conditions. However, similar to cell spreading and cell migration (Traynor and Kay, 2007), cytokinesis is also intimately linked to considerable remodeling of the plasma membrane (Neto et al., 2011). Remodeling is most prominently seen at the later stages of cytokinesis, during which fusion and fission of the curved lipid bilayer is required to constrict the mother cell in two. Because IBARa interacts preferentially with $PI(4,5)P_2$, which in turn has been shown to be enriched in the cleavage furrow and required for cytokinesis (at least in *Drosophila* and mammalian cells) (Field et al., 2005; Wong et al., 2005), we monitored the distribution of IBARa during cytokinesis by immunofluorescence microscopy. Consistent with previous work, the CV system was found to be fragmented in mitotic cells (Zhu et al., 1993; Gabriel et al., 1999). However, only in some cases did we find dispersed IBARa-containing vesicles in the vicinity of the cleavage furrow. This notwithstanding, during the final stage of cytokinesis, IBARa became highly concentrated in small foci at the cell periphery connecting the separating daughter cells. This enrichment appears to be transient, as it was not always observed. These findings therefore strongly suggest that IBARa primarily facilitates membrane fission and/or fusion of membrane sheets during mitotic cell division.

IBARa function in CV discharge

IBARa localizes most prominently at the CV membrane. The CV system is an osmoregulatory organelle composed of cisternae and interconnecting ducts (Gabriel et al., 1999). In regulating the osmolarity of the cytosol, the CV periodically fuses with the plasma membrane, forming pores to expel excess water from the cell, thus allowing cells to survive hypotonic stress (Heuser et al., 1993; Du et al., 2008). IBARa-null cells contain a substantially elevated number of CVs and show defects in osmoregulation. Despite the fact that numerous CV components, including vacuolar proton pumps (Heuser et al., 1993), actin, unconventional myosins (Zhu and Clarke, 1992; Heuser, 2006; Jung et al., 2009) and proteins implicated in membrane trafficking (Gerisch et al., 2002) have been identified, the molecular mechanism of CV discharge remains elusive. How could IBARa operate in this process? Of note, the F-BAR proteins MEGAP1 and MEGAP2 have also been previously shown to localize at the CV membrane (Heath and Insall, 2008). Interestingly, $MEGAP1^{-}/2^{-}$ double mutants empty their CVs less efficiently and have three times more CVs as

Journal of Cell Science (2014) 127, 1279–1292 doi:10.1242/jcs.140756

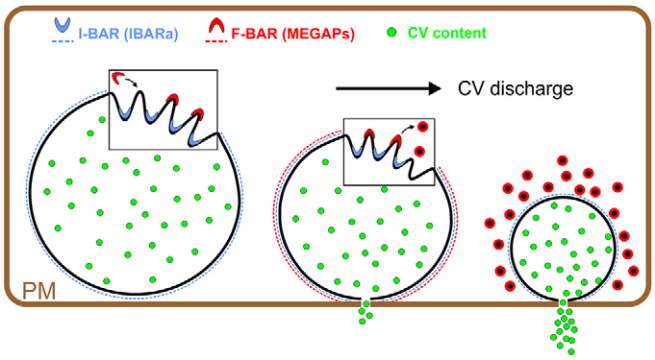

Fig. 7. Hypothetical model of IBARa function in CV discharge. After filling, the CV approaches the plasma membrane (PM) for discharge of the content through a porous channel. Provided that IBARa and MEGAPs (and possibly other F-BAR proteins) both act on the cytosolic side of the CV membrane, these proteins drive the formation of different curvatures (highlighted in the insets) and could cooperate in CV discharge by the coordinated removal of CV membrane during the process. The size of the CV is scaled up and its tubular network has been omitted for reasons of clarity.

compared to wild type. As assessed by time-lapse imaging, these proteins localize transiently to the CV membrane and subsequently fragment into smaller vesicles as the vacuole empties (Heath and Insall, 2008). Provided that IBARa, MEGAP1 and MEGAP2 (and possibly other F-BAR proteins) act on the same side of the CV membrane, we surmise that I-BAR and F-BAR proteins might synergize in CV discharge because the appearance of negative curvature is accompanied by positive curvature and vice versa. In our proposed model, we hypothesize that IBARa, residing most – if not all – of the time on the CV membrane, could serve to constitutively generate invaginations in the CV membrane, resulting in a highly folded surface. This, in turn, could facilitate the pinching of vesicles from the positively curved sites of the folded CV membrane by transiently binding F-BAR proteins, such as MEGAP1 and MEGAP2 (Fig. 7). Thus, IBARa might drive F-BAR-mediated vesicle formation to dismantle the CV membrane during acto-myosin-driven contraction. Future work will aim to address whether different types of F-BAR proteins, presumably containing different curvatures of their respective F-BAR domains, alternate in their entry on the CV to promote its discharge.

MATERIALS AND METHODS

Cell culture and transformation

The cultivation and transformation of *D. discoideum* AX2 wild-type (WT) cells and derived mutant strains were performed as described previously (Linkner et al., 2012).

Plasmids

The *ibrA*-cDNA (DictyBase ID DDB0266618) was amplified from a λgt11 cDNA library and inserted into the pJet1.2 vector (Fermentas) using the primers IBARa-H3U, 5′-GCGAAGCTTATGTCAAACGCTAAAAAACAAC-3′, and IBARa-BD, 5′-GCGGGATCCTACGTATTCAATATAAGTTGAAGG-3′. For construction of the *ibrA* gene-targeting vector, a 5′ *Bam*HI/*Pst*I fragment and a 3′ *Hin*dIII/*Sal*I fragment were amplified from genomic AX2 WT DNA by PCR. The primers used for the 5′ fragment were 5′-GCCGGATCCATGTCAAACGCTAAAAAACAACAAAATC-3′ and 5′-GCGCTGCAGAGAAAGTTAGAGGGGGAGGGGAGAGAGTG-3′, and the primers for the 3′ fragment were 5′-GCGAAGCTTGATAGAGATCAAATGAGACAAGATATT-3′ and 5′-GCGGTCGACTTATGCATATCAAATACGATATGCATC-3′. Both fragments were gel purified after cleavage with *BamHI*/*Pst*I and *Hin*dIII/*Sal*I, and were cloned into the corresponding sites of pLPBLP, which contains a Blasticidin S resistance cassette (Faix et al., 2004). The resulting vector was cleaved with *BamH*I and *Sal*I, and was used to disrupt the *ibrA* gene in WT cells. Null mutants were screened by PCR as described previously (Linkner et al., 2012).

For expression constructs, the coding sequence of IBARa (amino acids 1–259) was amplified by PCR using the primers IBARa-1BU, 5′-GCGGGATCCATGTCAAACGCTAAAAAACAAC-3′, and IBARa-259*s.d., 5′-GCGGTCGACTTATGCATATGAAATACGATATGCATC-3′. The coding sequence of the C-terminal fragment of IBARa (amino acids 225–357) was amplified by PCR using the primers IBARa-225BU, 5′-GCGGGATCCTTACCACTTGAAATGGAATCAATGATT-3′ and IBARa-357*s.d., 5′-GCGGTCGACTTATACGTATTCAATATAAGTTGAAGG-3′; both fragments carried *BamH*I and *Sal*I sites to facilitate cloning. The digested PCR fragments were inserted into the corresponding sites of pGEX-6P-1 (GE Healthcare). For the expression of N-terminal fusions to GFP, the coding sequence of IBARa was amplified by PCR using the primers IBARa-BU+2, 5′-GCGGGATCCGCATGTCAAACGCTAAAAAACAAC-3′, and IBARa-357*s.d. After digestion with *Bam*HI/*Sal*I, the PCR fragments were inserted into the corresponding sites of pDGFP-MCS-Neo (Faix et al., 2001). For C-terminal GFP fusion constructs, the coding sequence of IBARa was amplified by PCR using the primers IBARa-H3U, 5′-GCGAAGCTTAAAAATGTCAAACGCTAAAAAACAAC-3′, and IBARa-BD, 5′-GCGGGATCCTACGTATTCAATATAAGTTGAAGG-3′. After digestion with *Hind*III/*Bam*HI, the PCR fragments were inserted into the corresponding sites of pB15GFPXSac1A (Gräf et al., 2000). All constructs were verified by sequencing. The plasmids for expression of GFP–Dajumin, GFP–myosin-VII and csA-Rho50 were as described previously (Gabriel et al., 1999; Tuxworth et al., 2001; Mercanti et al., 2006).

Protein purification

IBARa (amino acids 1–259, also referred to herein as IBARa-N) and IBARa (amino acids 225–357) fragments were purified from *E. coli* host BL21 DE3 as an N-terminally GST-tagged fusion protein. Briefly, the fusion protein was first purified on glutathione sepharose (GE Healthcare), eluted with buffer A containing 20 mM Tris-HCl pH 8.0, 300 mM NaCl, 1 mM EDTA and 1 mM dithiothreitol (DTT), supplemented with 30 mM reduced glutathione. The GST-tag from IBARa-N was subsequently cleaved with PreScission protease (GE Healthcare). The resulting IBARa-N protein carries the extra amino acids GPLGS at its N-terminus. After cleavage, the protein fragments were separated by size-exclusion chromatography on a Superdex-S200 26/60 column (GE Healthcare) equilibrated with buffer A. The protein was then dialyzed three times against buffer B containing 20 mM HEPES pH 7.3, 300 mM NaCl, 1 mM DTT, 0.1 mM EDTA and 0.01% NaN_3 for crystallization. Selenomethionine-substituted protein for crystallization was expressed in the Met-auxotroph *E. coli* B831 as described previously (Hendrickson et al., 1990), and was purified as described above with the addition of 5 mM β-mercaptoethanol to all buffers used in purification and 2 mM DTT to the final storage buffer.

Generation of IBARa antibodies

Polyclonal antibodies were obtained by immunizing female white New Zealand rabbits with recombinant GST-tagged IBARa (amino acids 225–357) together with complete Freund's adjuvant (Sigma). The specificity of the antibodies for IBARa was assessed by western blotting.

Preparation of fluorescently labeled yeast particles

Saccharomyces cerevisiae were grown in shaking suspension in yeast peptone dextrose adenine (YPDA) medium at 30℃. For the generation of dumbbell-shaped yeast, 10 µg/ml nocodazole was added during the logarithmic growth phase and the cells were incubated for another 90 min to arrest them in telophase. Nocodazole-treated yeast (NTY) and untreated yeast cultures were pelleted and resuspended in distilled water, incubated at 100℃ for 20 min and labeled with tetramethylrhodamine isothiocyanate (TRITC), followed by vigorous washing to remove free dye. The cell density was adjusted to 5×10^8 cells/ml and aliquots were stored at −20℃.

Journal of Cell Science (2014) 127, 1279–1292 doi:10.1242/jcs.140756

Determination of growth rates, phagocytosis and pinocytosis

Quantitative fluid-phase uptake and the determination of growth rates on bacterial lawns and in shaken suspensions were performed as described previously (Dumontier et al., 2000). Phagocytosis assays were carried out as described previously (Maniak et al., 1995).

Osmotic shock treatment

Axenically grown cells were harvested at a density of not more than 5×10^6 cells/ml, washed in 17 mM Soerensen phosphate buffer (PB, pH 6.0) and transferred into double-distilled water (ddH_2O). The cell density was adjusted to 3×10^6 cells/ml and the cells were shaken in 25 ml of ddH_2O at 150 rpm at 23℃ for 24 h. After various lengths of incubation, the cells were diluted into PB and 100 cells/plate were plated on SM-agar together with a solution of *Klebsiella aerogenes*. Colonies were counted after incubation for 48 h at 23℃.

Microscopy

For imaging, axenically grown cells were seeded onto glass-bottom dishes (MatTek) and incubated in 17 mM phosphate-buffer (pH 6.1) for 1 h to reduce autofluorescence and to stimulate CV activity. The CVs of live cells were visualized with the lipophilic dye FM2-10 (Molecular Probes) as described previously (Heath and Insall, 2008), and were imaged using an Olympus Fluoview FV1000 confocal microscope (Olympus) at a rate of 1 frame every 5 s. The topography of the ventral cell surface, including filopodia and cell-to-substratum contacts, was imaged by RICM using a LSM 510 confocal microscope (Zeiss) and the 633-nm line of the He-Ne laser. Immunolabeling of fixed cells with polyclonal anti-IBARa antibodies or monoclonal anti-cortexillin antibody (241-71-3) was essentially performed as described previously (Faix et al., 2001). Endosomes were labelled with the monoclonal antibody H161 (Ravanel et al., 2001) and the CV marker csA-Rho50 was visualized with anti-csA monoclonal antibody 41-71-21 (Bertholdt et al., 1985). GFP was enhanced with Atto488-conjugated nanobodies (Chromotek). F-actin was visualized by fluorescent phalloidin (Molecular Probes), and DNA was stained with DAPI or TO-PRO-3 (Molecular Probes).

Retracting and protruding filopodia and discharging CVs were filmed with an Olympus IX-81 fluorescence microscope equipped with phase-contrast optics (Olympus) and a CoolSnap EZ camera (Photometrics) at a rate of 1 frame per second. For the latter experiment, the cells were allowed to adhere to 3-cm-diameter glass-bottom dishes (Ibidi) and were subsequently washed with PB and modestly compressed between a thin sheet of 1.5% agarose in PB and the glass surface essentially as described previously (Fukui et al., 1987). The CV discharge rate was quantified as follows: randomly picked CVs of WT and mutant cells were selected and their diameters were determined for each frame. The corresponding volumes were calculated and plotted over time. The centroid of each single curve was translated into the origin and thereby pooled into a single data set for each strain. Finally, the respective CV discharge rates were determined by linear regression of the data.

Vesicle cosedimentation assays

Large unilamellar vesicles were prepared as described previously (Saarikangas et al., 2009), and vesicle cosedimentation assays were performed as described previously (Zhao et al., 2010). The final concentrations of IBARa-N and liposomes were 3 µM and 1 mM, respectively, in buffer containing 20 mM HEPES pH 7.5 and 100 mM NaCl buffer.

Negative stain electron microscopy

Samples for transmission electron microscopy were prepared by mixing 5 µM proteins with 200 µM unilamellar vesicles (Ø=400 nm) in 20 mM Tris-HCl pH 7.5, 100 mM NaCl at room temperature for 15 min. This mixture was applied to the glow-discharged collodion- and carbon-coated copper grids and stained with 3% uranyl acetate. At each step, excess solution was removed by filter paper. The membrane morphologies were examined with a Tecnai 20 FEG electron microscope (FEI Corp.) operating at 80 kV. Images were recorded with a 4k×4k Ultrascan 4000 CCD camera (Gatan Corp.) with a magnification of ×13,000.

Tubulation of giant unilamellar liposomes

Giant unilamellar vesicles (GUVs) were prepared as described (Saarikangas et al., 2009). The lipid composition of the GUVs was POPC:POPE:POPS:PIP_2:TopFluor-PIP_2 (50:20:20:9:1). GUVs were mixed with the same osmolarity buffer (approx. 200 mM glucose in 5 mM HEPES pH 7.5 buffer) at a 1:3 ratio prior to imaging. The total volume of the samples during imaging was 100 µl and the final concentration of protein added to the GUVs was 1 µM. 1-Palmitoyl-2-oleoyl-*sn*-glycero-3-phosphatidylcholine (POPC), 1-palmitoyl-2-oleoyl-*sn*-glycero-3-phosphatidylethanol-amine (POPE), 1-palmitoyl-2-oleoyl-*sn*-glycero-3-phosphatidylserine (POPS) were purchased from Avanti Polar Lipids.

BODIPY quenching experiment

The fluorescence measurements were performed in quartz cuvettes with a 3-mm path length. Fluorescence spectra were measured with a PerkinElmer LS 55 spectrometer (Perkin-Elmer). BODIPY-FL–$PI(4,5)P_2$ fluorescence was excited at 495 nm and the emission spectra were recorded from 503 to 530 nm in the presence of different concentrations of protein. Emission and excitation band passes were set at 4 nm. All experiments were carried out in 20 mM HEPES, 100 mM NaCl pH 7.5 at room temperature. The percentage of quenching was calculated as: % quenching$=(1-F/F_0)\times100$, where F is the fluorescence intensity of BODIPY-FL–$PI(4,5)P_2$ in the presence of protein, and F_0 is the fluorescence intensity of BODIPY-FL–$PI(4,5)P_2$ in the absence of protein. The lipid composition was POPC:POPE:POPS:$PI(4,5)P_2$:BODIPY-FL–$PI(4,5)P_2$ at a ratio of 50:20:20:9.5:0.5 and the lipid concentration was 30 µM. $PI(4,5)P_2$ was purchased from Avanti Polar Lipids. BODIPY-FL–$PI(4,5)P_2$ was purchased from Echelon Biosciences.

Fluorescence anisotropy of DPH

The lipid composition was POPC:POPE:POPS:$PI(4,5)P_2$:DPH at a ratio of 50:20:20:10:0.2 and the lipid concentration used was 40 µM. 1,6-diphenyl-1,3,5-hexatriene (DPH) was obtained from Invitrogen. Fluorescence anisotropy for DPH was measured with a PerkinElmer LS 55 spectrometer. The excitation was set at 360 nm and emission at 450 nm, using 10-nm bandwidths. The experiments were carried out in 20 mM HEPES and 100 mM NaCl pH 7.5 at room temperature.

Crystallization and structure determination

Crystals of selenomethionine-substituted protein were obtained in hanging-drop geometry using 20% PEG3350, 0.25 M CH_3COONH_4 and 15% (v/v) glycerol as the reservoir solution. 1.5 µl of reservoir was added to an equal volume of IBARa-N (10 mg/ml) in storage buffer supplemented with 2 mM Tris-(2-carboxyethyl)phosphine (TCEP) and incubated at 20℃. Crystals were backsoaked in mother liquor containing 20% (v/v) ethylene glycol for cryoprotection. Data collection at the synchrotron was carried out at 100 K at the selenium peak wavelength determined by a fluorescence scan. Diffraction data were indexed, integrated and scaled using the XDS-package (Kabsch, 1993). Phases were obtained by autoSHARP (Vonrhein et al., 2007). Density modification was performed using PIRATE and PARROT (Zhang et al., 1997). The high-resolution data allowed automatic model building using buccaneer (Cowtan, 2006). The preliminary model was refined in cyclic rounds of manual model building in COOT (Emsley and Cowtan, 2004) and refinement was performed using PHENIX (Adams et al., 2010). The final model showed no outliers in the Ramachandran plot and reasonable *R*-factors and geometries. Atomic coordinates and structure factors were deposited in the Protein Data Bank with accession number 4NQI. The data collection and refinement statistics are listed in Table 1. Figures were prepared with PyMOL (DeLano, 2008; http://www.pymol.org).

Small-angle X-ray scattering

Small-angle X-ray scattering data were collected at EMBL/DESY P12 and X33 (Hamburg, Germany) and ESRF ID14-3 (Grenoble, France). Protein samples were measured at different protein concentrations between 1 and 9 mg/ml. The scattering data of the running buffer from

size exclusion chromatography were used for buffer correction. The scattering data were analyzed using the ATSAS package (Petoukhov et al., 2007) as described (Putnam et al., 2007). No particle interaction or aggregation could be detected in the observed concentration range (c.f. supplementary material Fig. S7). The radius of gyration (R_g) and the extrapolated scattering intensity at zero angle for molecular mass determination (I_o) were obtained from Guinier-plot analysis [log(I(s) versus s^2] with $sR_g < 1.3$ (Putnam et al., 2007). Calculation of the theoretical scattering curve from the IBARa-N crystal structure was performed using CRYSOL (Svergun et al., 1995) (ZITAT). Sets of 16 independent *ab initio* models were each calculated using GASBOR (Svergun et al., 2001) and DAMMIF (Franke and Svergun, 2009), and were filtered and averaged using DAMAVER (Volkov and Svergun, 2003). Figures were prepared using SITUS (Wriggers and Chacón, 2001) and UCSF Chimera (Pettersen et al., 2004).

Acknowledgements
We thank the staff of X06SA at the Swiss Light Source (Villigen), ESRF ID14-3 (Grenoble) and DESY/EMBL X33/P12 (Hamburg) for help and support during data collection, and M. Winterhoff and J. Greipel (MHH, Hannover) for stimulating discussions and help during image processing. We further thank A. Müller-Taubenberger (LMU, Munich) for plasmid pDGFP–Dajumin, M. Titus (University of Minnesota, MN) for pTX-GFP–Ddmyosin-VII plasmid and R. Gräf (University of Potsdam, Potsdam) for plasmid pB15GFPXSac1A. We also thank the Dicty Stock Center for csA-Rho50 expression construct pFL674 and its depositor F. Letourneur (University of Lyon, Lyon). We are grateful to G. Gerisch (MPI, Martinsried) for providing anti-csA antibody.

Competing interests
The authors declare no competing interests.

Author Contribution
J.L., G.W., H.X., B.J., P.W., A.J. and J.F. performed experiments. J.L., G.W., P.L. and J.F. designed experiments and wrote the manuscript.

Funding
This work was supported by grants from the Deutsche Forschungsgemeinschaft [grant numbers 330/5-1 to J.F., GRK1721, 3717/2-1 to G.W.]; and from the Academy of Finland [grant number 137946 to P.L.].

Supplementary material
Supplementary material available online at
http://jcs.biologists.org/lookup/suppl/doi:10.1242/jcs.140756/-/DC1

References
Adams, P. D., Afonine, P. V., Bunkóczi, G., Chen, V. B., Davis, I. W., Echols, N., Headd, J. J., Hung, L. W., Kapral, G. J., Grosse-Kunstleve, R. W. et al. (2010). PHENIX: a comprehensive Python-based system for macromolecular structure solution. *Acta Crystallogr. D Biol. Crystallogr.* **66**, 213-221.

Baker, N. A., Sept, D., Joseph, S., Holst, M. J. and McCammon, J. A. (2001). Electrostatics of nanosystems: application to microtubules and the ribosome. *Proc. Natl. Acad. Sci. USA* **98**, 10037-10041.

Bertholdt, G., Stadler, J., Bozzaro, S., Fichtner, B. and Gerisch, G. (1985). Carbohydrate and other epitopes of the contact site A glycoprotein of Dictyostelium discoideum as characterized by monoclonal antibodies. *Cell Differ.* **16**, 187-202.

Biyasheva, A., Svitkina, T., Kunda, P., Baum, B. and Borisy, G. (2004). Cascade pathway of filopodia formation downstream of SCAR. *J. Cell Sci.* **117**, 837-848.

Carlson, B. R., Lloyd, K. E., Kruszewski, A., Kim, I. H., Rodriguiz, R. M., Heindel, C., Faytell, M., Dudek, S. M., Wetsel, W. C. and Soderling, S. H. (2011). WRP/srGAP3 facilitates the initiation of spine development by an inverse F-BAR domain, and its loss impairs long-term memory. *J. Neurosci.* **31**, 2447-2460.

Chauhan, B. K., Disanza, A., Choi, S. Y., Faber, S. C., Lou, M., Beggs, H. E., Scita, G., Zheng, Y. and Lang, R. A. (2009). Cdc42- and IRSp53-dependent contractile filopodia tether presumptive lens and retina to coordinate epithelial invagination. *Development* **136**, 3657-3667.

Clarke, M., Engel, U., Giorgione, J., Müller-Taubenberger, A., Prassler, J., Veltman, D. and Gerisch, G. (2010). Curvature recognition and force generation in phagocytosis. *BMC Biol.* **8**, 154.

Cowtan, K. (2006). The Buccaneer software for automated model building. 1. Tracing protein chains. *Acta Crystallogr. D Biol. Crystallogr.* **62**, 1002-1011.

Damer, C. K., Bayeva, M., Hahn, E. S., Rivera, J. and Socec, C. I. (2005). Copine A, a calcium-dependent membrane-binding protein, transiently localizes to the plasma membrane and intracellular vacuoles in Dictyostelium. *BMC Cell Biol.* **6**, 46.

Damer, C. K., Bayeva, M., Kim, P. S., Ho, L. K., Eberhardt, E. S., Socec, C. I., Lee, J. S., Bruce, E. A., Goldman-Yassen, A. E. and Naliboff, L. C. (2007). Copine A is required for cytokinesis, contractile vacuole function, and development in Dictyostelium. *Eukaryot. Cell* **6**, 430-442.

de Groot, J. C., Schlüter, K., Carius, Y., Quedenau, C., Vingadassalom, D., Faix, J., Weiss, S. M., Reichelt, J., Standfuss-Gabisch, C., Lesser, C. F. et al. (2011). Structural basis for complex formation between human IRSp53 and the translocated intimin receptor Tir of enterohemorrhagic E. coli. *Structure* **19**, 1294-1306.

DeLano, W. L. (2008). pyMOL. DeLano Scientific LLC, Palo Alto, CA, USA. http://www.pymol.org.

Disanza, A., Bisi, S., Winterhoff, M., Milanesi, F., Ushakov, D. S., Kast, D., Marighetti, P., Romet-Lemonne, G., Müller, H. M., Nickel, W. et al. (2013). CDC42 switches IRSp53 from inhibition of actin growth to elongation by clustering of VASP. *EMBO J.* **32**, 2735-2750.

Du, F., Edwards, K., Shen, Z., Sun, B., De Lozanne, A., Briggs, S. and Firtel, R. A. (2008). Regulation of contractile vacuole formation and activity in Dictyostelium. *EMBO J.* **27**, 2064-2076.

Dumontier, M., Höcht, P., Mintert, U. and Faix, J. (2000). Rac1 GTPases control filopodia formation, cell motility, endocytosis, cytokinesis and development in *Dictyostelium. J. Cell Sci.* **113**, 2253-2265.

Eichinger, L., Pachebat, J. A., Glöckner, G., Rajandream, M. A., Sucgang, R., Berriman, M., Song, J., Olsen, R., Szafranski, K., Xu, Q. et al. (2005). The genome of the social amoeba Dictyostelium discoideum. *Nature* **435**, 43-57.

Emsley, P. and Cowtan, K. (2004). Coot: model-building tools for molecular graphics. *Acta Crystallogr. D Biol. Crystallogr.* **60**, 2126-2132.

Faix, J., Weber, I., Mintert, U., Köhler, J., Lottspeich, F. and Marriott, G. (2001). Recruitment of cortexillin into the cleavage furrow is controlled by Rac1 and IQGAP-related proteins. *EMBO J.* **20**, 3705-3715.

Faix, J., Kreppel, L., Shaulsky, G., Schleicher, M. and Kimmel, A. R. (2004). A rapid and efficient method to generate multiple gene disruptions in Dictyostelium discoideum using a single selectable marker and the Cre-loxP system. *Nucleic Acids Res.* **32**, e143.

Field, S. J., Madson, N., Kerr, M. L., Galbraith, K. A. A., Kennedy, C. E., Tahiliani, M., Wilkins, A. and Cantley, L. C. (2005). PtdIns(4,5)P2 functions at the cleavage furrow during cytokinesis. *Curr. Biol.* **15**, 1407-1412.

Franke, D. and Svergun, D. I. (2009). DAMMIF, a program for rapid ab-initio shape determination in small-angle scattering. *J. Appl. Crystallogr.* **42**, 342-346.

Frost, A., Perera, R., Roux, A., Spasov, K., Destaing, O., Egelman, E. H., De Camilli, P. and Unger, V. M. (2008). Structural basis of membrane invagination by F-BAR domains. *Cell* **132**, 807-817.

Frost, A., Unger, V. M. and De Camilli, P. (2009). The BAR domain superfamily: membrane-molding macromolecules. *Cell* **137**, 191-196.

Fukui, Y. and Inoué, S. (1991). Cell division in Dictyostelium with special emphasis on actomyosin organization in cytokinesis. *Cell Motil. Cytoskeleton* **18**, 41-54.

Fukui, Y., Yumura, S. and Yumura, T. K. (1987). Agar-overlay immunofluorescence: high-resolution studies of cytoskeletal components and their changes during chemotaxis. *Methods Cell Biol.* **28**, 347-356.

Gabriel, D., Hacker, U., Köhler, J., Müller-Taubenberger, A., Schwartz, J. M., Westphal, M. and Gerisch, G. (1999). The contractile vacuole network of Dictyostelium as a distinct organelle: its dynamics visualized by a GFP marker protein. *J. Cell Sci.* **112**, 3995-4005.

Gerald, N. J., Siano, M. and De Lozanne, A. (2002). The Dictyostelium LvsA protein is localized on the contractile vacuole and is required for osmoregulation. *Traffic* **3**, 50-60.

Gerisch, G., Heuser, J. and Clarke, M. (2002). Tubular-vesicular transformation in the contractile vacuole system of Dictyostelium. *Cell Biol. Int.* **26**, 845-852.

Goh, W. I., Sudhaharan, T., Lim, K. B., Sem, K. P., Lau, C. L. and Ahmed, S. (2011). Rif-mDia1 interaction is involved in filopodium formation independent of Cdc42 and Rac effectors. *J. Biol. Chem.* **286**, 13681-13694.

Gräf, R., Daunderer, C. and Schliwa, M. (2000). Dictyostelium DdCP224 is a microtubule-associated protein and a permanent centrosomal resident involved in centrosome duplication. *J. Cell Sci.* **113**, 1747-1758.

Guerrier, S., Coutinho-Budd, J., Sassa, T., Gresset, A., Jordan, N. V., Chen, K., Jin, W. L., Frost, A. and Polleux, F. (2009). The F-BAR domain of srGAP2 induces membrane protrusions required for neuronal migration and morphogenesis. *Cell* **138**, 990-1004.

Heath, R. J. and Insall, R. H. (2008). Dictyostelium MEGAPs: F-BAR domain proteins that regulate motility and membrane tubulation in contractile vacuoles. *J. Cell Sci.* **121**, 1054-1064.

Hendrickson, W. A., Horton, J. R. and LeMaster, D. M. (1990). Selenomethionyl proteins produced for analysis by multiwavelength anomalous diffraction (MAD): a vehicle for direct determination of three-dimensional structure. *EMBO J.* **9**, 1665-1672.

Heuser, J. (2006). Evidence for recycling of contractile vacuole membrane during osmoregulation in Dictyostelium amoebae – a tribute to Günther Gerisch. *Eur. J. Cell Biol.* **85**, 859-871.

Heuser, J., Zhu, Q. and Clarke, M. (1993). Proton pumps populate the contractile vacuoles of Dictyostelium amoebae. *J. Cell Biol.* **121**, 1311-1327.

Jung, G., Titus, M. A. and Hammer, J. A., III (2009). The Dictyostelium type V myosin MyoJ is responsible for the cortical association and motility of contractile vacuole membranes. *J. Cell Biol.* **186**, 555-570.

Kabsch, W. (1993). Automatic processing of rotation diffraction data from crystals of initially unknown symmetry and cell constants. *J. Appl. Crystallogr.* **26**, 795-800.
Keren, K. (2011). Membrane tension leads the way. *Proc. Natl. Acad. Sci. USA* **108**, 14379-14380.
Kim, M. H., Choi, J., Yang, J., Chung, W., Kim, J. H., Paik, S. K., Kim, K., Han, S., Won, H., Bae, Y. S. et al. (2009). Enhanced NMDA receptor-mediated synaptic transmission, enhanced long-term potentiation, and impaired learning and memory in mice lacking IRSp53. *J. Neurosci.* **29**, 1586-1595.
Krugmann, S., Jordens, I., Gevaert, K., Driessens, M., Vandekerckhove, J. and Hall, A. (2001). Cdc42 induces filopodia by promoting the formation of an IRSp53:Mena complex. *Curr. Biol.* **11**, 1645-1655.
Kwak, E., Gerald, N., Larochelle, D. A., Vithalani, K. K., Niswonger, M. L., Maready, M. and De Lozanne, A. (1999). LvsA, a protein related to the mouse beige protein, is required for cytokinesis in Dictyostelium. *Mol. Biol. Cell* **10**, 4429-4439.
Lee, Y. G., Macoska, J. A., Korenchuk, S. and Pienta, K. J. (2002). MIM, a potential metastasis suppressor gene in bladder cancer. *Neoplasia* **4**, 291-294.
Lee, S. H., Kerff, F., Chereau, D., Ferron, F., Klug, A. and Dominguez, R. (2007). Structural basis for the actin-binding function of missing-in-metastasis. *Structure* **15**, 145-155.
Linkner, J., Nordholz, B., Junemann, A., Winterhoff, M. and Faix, J. (2012). Highly effective removal of floxed Blasticidin S resistance cassettes from Dictyostelium discoideum mutants by extrachromosomal expression of Cre. *Eur. J. Cell Biol.* **91**, 156-160.
Maniak, M., Rauchenberger, R., Albrecht, R., Murphy, J. and Gerisch, G. (1995). Coronin involved in phagocytosis: dynamics of particle-induced relocalization visualized by a green fluorescent protein Tag. *Cell* **83**, 915-924.
Mattila, P. K., Pykäläinen, A., Saarikangas, J., Paavilainen, V. O., Vihinen, H., Jokitalo, E. and Lappalainen, P. (2007). Missing-in-metastasis and IRSp53 deform PI(4,5)P2-rich membranes by an inverse BAR domain-like mechanism. *J. Cell Biol.* **176**, 953-964.
Mercanti, V., Blanc, C., Lefkir, Y., Cosson, P. and Letourneur, F. (2006). Acidic clusters target transmembrane proteins to the contractile vacuole in Dictyostelium cells. *J. Cell Sci.* **119**, 837-845.
Millard, T. H., Bompard, G., Heung, M. Y., Dafforn, T. R., Scott, D. J., Machesky, L. M. and Fütterer, K. (2005). Structural basis of filopodia formation induced by the IRSp53/MIM homology domain of human IRSp53. *EMBO J.* **24**, 240-250.
Nakagawa, H., Miki, H., Nozumi, M., Takenawa, T., Miyamoto, S., Wehland, J. and Small, J. V. (2003). IRSp53 is colocalised with WAVE2 at the tips of protruding lamellipodia and filopodia independently of Mena. *J. Cell Sci.* **116**, 2577-2583.
Neto, H., Collins, L. L. and Gould, G. W. (2011). Vesicle trafficking and membrane remodelling in cytokinesis. *Biochem. J.* **437**, 13-24.
Neujahr, R., Heizer, C. and Gerisch, G. (1997). Myosin II-independent processes in mitotic cells of Dictyostelium discoideum: redistribution of the nuclei, re-arrangement of the actin system and formation of the cleavage furrow. *J. Cell Sci.* **110**, 123-137.
Peter, B. J., Kent, H. M., Mills, I. G., Vallis, Y., Butler, P. J., Evans, P. R. and McMahon, H. T. (2004). BAR domains as sensors of membrane curvature: the amphiphysin BAR structure. *Science* **303**, 495-499.
Petoukhov, M. V., Konarev, P. V., Kikhney, A. G. and Svergun, D. I. (2007). ATSAS 2.1 – towards automated and web-supported small-angle scattering data analysis. *J. Appl. Crystallogr.* **40**, s223-s228.
Pettersen, E. F., Goddard, T. D., Huang, C. C., Couch, G. S., Greenblatt, D. M., Meng, E. C. and Ferrin, T. E. (2004). UCSF Chimera – a visualization system for exploratory research and analysis. *J. Comput. Chem.* **25**, 1605-1612.
Putnam, C. D., Hammel, M., Hura, G. L. and Tainer, J. A. (2007). X-ray solution scattering (SAXS) combined with crystallography and computation: defining accurate macromolecular structures, conformations and assemblies in solution. *Q. Rev. Biophys.* **40**, 191-285.
Pykäläinen, A., Boczkowska, M., Zhao, H., Saarikangas, J., Rebowski, G., Jansen, M., Hakanen, J., Koskela, E. V., Peränen, J., Vihinen, H. et al. (2011). Pinkbar is an epithelial-specific BAR domain protein that generates planar membrane structures. *Nat. Struct. Mol. Biol.* **18**, 902-907.
Qualmann, B., Koch, D. and Kessels, M. M. (2011). Let's go bananas: revisiting the endocytic BAR code. *EMBO J.* **30**, 3501-3515.
Ravanel, K., de Chassey, B., Cornillon, S., Benghezal, M., Zulianello, L., Gebbie, L., Letourneur, F. and Cosson, P. (2001). Membrane sorting in the endocytic and phagocytic pathway of Dictyostelium discoideum. *Eur. J. Cell Biol.* **80**, 754-764.
Saarikangas, J., Hakanen, J., Mattila, P. K., Grumet, M., Salminen, M. and Lappalainen, P. (2008). ABBA regulates plasma-membrane and actin dynamics to promote radial glia extension. *J. Cell Sci.* **121**, 1444-1454.
Saarikangas, J., Zhao, H., Pykäläinen, A., Laurinmäki, P., Mattila, P. K., Kinnunen, P. K., Butcher, S. J. and Lappalainen, P. (2009). Molecular mechanisms of membrane deformation by I-BAR domain proteins. *Curr. Biol.* **19**, 95-107.
Saarikangas, J., Zhao, H. and Lappalainen, P. (2010). Regulation of the actin cytoskeleton-plasma membrane interplay by phosphoinositides. *Physiol. Rev.* **90**, 259-289.
Saarikangas, J., Mattila, P. K., Varjosalo, M., Bovellan, M., Hakanen, J., Calzada-Wack, J., Tost, M., Jennen, L., Rathkolb, B., Hans, W. et al. (2011). Missing-in-metastasis MIM/MTSS1 promotes actin assembly at intercellular junctions and is required for integrity of kidney epithelia. *J. Cell Sci.* **124**, 1245-1255.
Sawallisch, C., Berhörster, K., Disanza, A., Mantoani, S., Kintscher, M., Stoenica, L., Dityatev, A., Sieber, S., Kindler, S., Morellini, F. et al. (2009). The insulin receptor substrate of 53 kDa (IRSp53) limits hippocampal synaptic plasticity. *J. Biol. Chem.* **284**, 9225-9236.
Scita, G., Confalonieri, S., Lappalainen, P. and Suetsugu, S. (2008). IRSp53: crossing the road of membrane and actin dynamics in the formation of membrane protrusions. *Trends Cell Biol.* **18**, 52-60.
Suetsugu, S., Murayama, K., Sakamoto, A., Hanawa-Suetsugu, K., Seto, A., Oikawa, T., Mishima, C., Shirouzu, M., Takenawa, T. and Yokoyama, S. (2006a). The RAC binding domain/IRSp53-MIM homology domain of IRSp53 induces RAC-dependent membrane deformation. *J. Biol. Chem.* **281**, 35347-35358.
Suetsugu, S., Kurisu, S., Oikawa, T., Yamazaki, D., Oda, A. and Takenawa, T. (2006b). Optimization of WAVE2 complex-induced actin polymerization by membrane-bound IRSp53, $PIP_{(3)}$, and Rac. *J. Cell Biol.* **173**, 571-585.
Svergun, D. I., Barberato, C. and Koch, M. H. J. (1995). CRYSOL – a program to evaluate x-ray solution scattering of biological macromolecules from atomic coordinates. *J. Appl. Crystallogr.* **28**, 768-773.
Svergun, D. I., Petoukhov, M. V. and Koch, M. H. J. (2001). Determination of domain structure of proteins from X-ray solution scattering. *Biophys. J.* **80**, 2946-2953.
Traynor, D. and Kay, R. R. (2007). Possible roles of the endocytic cycle in cell motility. *J. Cell Sci.* **120**, 2318-2327.
Tuxworth, R. I., Weber, I., Wessels, D., Addicks, G. C., Soll, D. R., Gerisch, G. and Titus, M. A. (2001). A role for myosin VII in dynamic cell adhesion. *Curr. Biol.* **11**, 318-329.
Vaggi, F., Disanza, A., Milanesi, F., Di Fiore, P. P., Menna, E., Matteoli, M., Gov, N. S., Scita, G. and Ciliberto, A. (2011). The Eps8/IRSp53/VASP network differentially controls actin capping and bundling in filopodia formation. *PLOS Comput. Biol.* **7**, e1002088.
Veltman, D. M., Auciello, G., Spence, H. J., Machesky, L. M., Rappoport, J. Z. and Insall, R. H. (2011). Functional analysis of Dictyostelium IBARa reveals a conserved role of the I-BAR domain in endocytosis. *Biochem. J.* **436**, 45-52.
Volkov, V. V. and Svergun, D. I. (2003). Uniqueness of ab-initio shape determination in small-angle scattering. *J. Appl. Crystallogr.* **36**, 860-864.
Vonrhein, C., Blanc, E., Roversi, P. and Bricogne, G. (2007). Automated structure solution with autoSHARP. *Methods Mol. Biol.* **364**, 215-230.
Wasiak, S., Quinn, C. C., Ritter, B., de Heuvel, E., Baranes, D., Plomann, M. and McPherson, P. S. (2001). The Ras/Rac guanine nucleotide exchange factor mammalian Son-of-sevenless interacts with PACSIN 1/syndapin I, a regulator of endocytosis and the actin cytoskeleton. *J. Biol. Chem.* **276**, 26622-26628.
Weber, I., Gerisch, G., Heizer, C., Murphy, J., Badelt, K., Stock, A., Schwartz, J. M. and Faix, J. (1999). Cytokinesis mediated through the recruitment of cortexillins into the cleavage furrow. *EMBO J.* **18**, 586-594.
Wong, R., Hadjiyanni, I., Wei, H.-C., Polevoy, G., McBride, R., Sem, K.-P. and Brill, J. A. (2005). PIP2 hydrolysis and calcium release are required for cytokinesis in Drosophila spermatocytes. *Curr. Biol.* **15**, 1401-1406.
Wriggers, W. and Chacón, P. (2001). Using situs for the registration of protein structures with low-resolution bead models from x-ray solution scattering. *J. Appl. Crystallogr.* **34**, 773-776.
Yu, D., Zhan, X. H., Zhao, X. F., Williams, M. S., Carey, G. B., Smith, E., Scott, D., Zhu, J., Guo, Y., Cherukuri, S. et al. (2012). Mice deficient in MIM expression are predisposed to lymphomagenesis. *Oncogene* **31**, 3561-3568.
Zaritsky, A., Parola, A. H., Abdah, M. and Masalha, H. (1985). Homeoviscous adaptation, growth rate, and morphogenesis in bacteria. *Biophys. J.* **48**, 337-339.
Zhang, K. Y., Cowtan, K. and Main, P. (1997). Combining constraints for electron-density modification. *Methods Enzymol.* **277**, 53-64.
Zhao, H., Hakala, M. and Lappalainen, P. (2010). ADF/cofilin binds phosphoinositides in a multivalent manner to act as a PIP(2)-density sensor. *Biophys. J.* **98**, 2327-2336.
Zhu, Q. and Clarke, M. (1992). Association of calmodulin and an unconventional myosin with the contractile vacuole complex of Dictyostelium discoideum. *J. Cell Biol.* **118**, 347-358.
Zhu, Q., Liu, T. and Clarke, M. (1993). Calmodulin and the contractile vacuole complex in mitotic cells of Dictyostelium discoideum. *J. Cell Sci.* **104**, 1119-1127.

Journal of Cell Science